Check for updates

ADVANCING EARTH AND SPACE SCIENCES

JGR Solid Earth

RESEARCH ARTICLE

10.1029/2025JB031323

Key Points:

- Optimized localization of seismic events during mine flooding reveals seismicity 300 m below the mining level centered around pillar zones
- Geomechanical simulation based on mine architecture and regional stress explains observed seismicity by stress arching and reduced effective stresses below pillar zones
- Flooding-induced seismicity does not occur on larger natural faults in the mine Heinrich-Robert

Supporting Information:

Supporting Information may be found in the online version of this article.

Correspondence to:

T. Niederhuber,
thomas.niederhuber@kit.edu

Citation:

Niederhuber, T., Rische, M., Müller, B., Röckel, T., Allgaier, F., Fischer, K. D., et al. (2025). Geomechanics of flooding-induced microseismicity—implications for post-mining environments. *Journal of Geophysical Research: Solid Earth*, *130*, e2025JB031323. https://doi.org/10.1029/2025JB031323

Received 6 FEB 2025
Accepted 31 AUG 2025

Author Contributions:

Conceptualization: Thomas Niederhuber, Martina Rische, Birgit Müller
Data curation: Thomas Niederhuber, Martina Rische
Formal analysis: Thomas Niederhuber, Martina Rische, Birgit Müller
Funding acquisition: Birgit Müller, Kasper D. Fischer, Wolfgang Friederich
Investigation: Thomas Niederhuber, Martina Rische, Birgit Müller, Thomas Röckel
Methodology: Thomas Niederhuber, Martina Rische, Birgit Müller, Thomas Röckel

© 2025. The Author(s).
This is an open access article under the terms of the Creative Commons Attribution License, which permits use, distribution and reproduction in any medium, provided the original work is properly cited.

Geomechanics of Flooding-Induced Microseismicity—Implications for Post-Mining Environments

Thomas Niederhuber[1], Martina Rische[2], Birgit Müller[1], Thomas Röckel[3], Felix Allgaier[4], Kasper D. Fischer[2], Frank Schilling[1], and Wolfgang Friederich[2]

[1]Division of Technical Petrophysics, Institute of Applied Geosciences, Karlsruhe Institute of Technology, Karlsruhe, Germany, [2]Institute of Geology, Mineralogy and Geophysics, Ruhr-University, Bochum, Germany, [3]Piewak & Partner GmbH, Bayreuth, Germany, [4]Division of Structural Geology, Institute of Applied Geosciences, Karlsruhe Institute of Technology, Karlsruhe, Germany

Abstract Seismicity related to mining has gained considerable public attention in the last decades and is one of the reasons for mine closures in Germany. The seismicity in the Ruhr coal mining district of Germany has been monitored by different regional and (temporal) local networks and is classified as purely mining-induced without evidence for movement of major geological faults due to the contemporary tectonic stress field. During active mining, water was continuously pumped out of the mine to enable safe mining conditions. Mine closure was followed by a seismic gap. When pumping was reduced the mines were gradually flooded and microseismicity developed. This study investigates flooding-induced seismicity at the Heinrich Robert mine in the Eastern Ruhr coal district, where water levels rise from ∼1,150 m to ∼380 m depth as part of post-mining flooding operations. By applying event relocalization methods we detected concentrations of microseismicity at about 300 m below the lowest mine levels, and there especially in sections with pillars above. Classical diffusion models cannot be applied due to the non-linearities in the increase of pore pressure and water volume, different flow processes and the heterogeneity of the subsurface. We performed 3D numerical geomechanical modeling for different mine geometries, hydraulic behaviors and regional state of stress. Our results show that flooding-induced seismicity in mines is less influenced by the ambient stress state and the flooding water volume. Instead, the locations, the temporal evolution and the segments of potential fault reactivation during flooding are controlled by a combination of local stress concentrations in pillar zones below the lowest mining level and pore pressure rise. Both are governed by a complex mine geometry and the hydraulic connections therein. Our findings support that the magnitude of flooding-related earthquakes is controlled and limited by the size of critical stress concentrations and thus the dimensions of the mined panels.

Plain Language Summary In recent decades, people have become aware of the problems caused by earthquakes related to mining. These issues have resulted in the closure of mines in Germany. During the operation of mines in the Ruhr coal mining area of Germany, many earthquakes were recorded, while water was pumped out of the mines. After the mine closed, seismic activity decreased until flooding began. This study examines the earthquakes caused by flooding in the Heinrich-Robert mine. After mining ceased, the water level was around −1,150 m, and it is expected to flood up to a level of −380 m. Our research revealed significant seismic activity at approximately 300 m below the lowest mine levels, primarily under the pillar sections. We created a simple computer model of the mine. Using this, we demonstrated how stress increases beneath the pillars and how flooding can lead to failure. We also found that the size and shape of the mine openings affect where these stresses form. Therefore, the design of the mine can influence where, when and how strong these earthquakes might be.

1. Introduction

Globally, a vast number of large-scale underground facilities—primarily coal, metal ore, and other mineral mines—are either in active operation, in the process of decommissioning, or undergoing transitional phases. Each year, a significant proportion of these mines are closed and subsequently flooded. In the United States, the number of active underground coal mines has declined from 654 to 185 over the past 20 years (U.S. Energy Information Administration, 2023). Similarly, hard coal production in the European Union has decreased by 82% over the past 30 years (Eurostat, 2024). In parallel, the global demand for critical minerals is increasing, driven by the deployment of renewable energy technologies essential for the energy transition (e.g., Hund et al., 2020;

Project administration: Wolfgang Friederich
Resources: Frank Schilling, Wolfgang Friederich
Software: Thomas Niederhuber, Martina Rische, Kasper D. Fischer
Supervision: Birgit Müller, Kasper D. Fischer, Frank Schilling, Wolfgang Friederich
Validation: Thomas Röckel, Kasper D. Fischer
Visualization: Thomas Niederhuber, Martina Rische
Writing – original draft: Thomas Niederhuber, Martina Rische, Birgit Müller
Writing – review & editing: Thomas Niederhuber, Martina Rische, Birgit Müller, Thomas Röckel, Felix Allgaier, Kasper D. Fischer, Frank Schilling, Wolfgang Friederich

IEA, 2024). This demand has led to the reopening of formerly abandoned mines and the development of new mining projects. Beyond conventional resource extraction, disused underground spaces are increasingly being repurposed for innovative energy-related applications or waste storage. These include hydroelectric energy storage using underground pumped-storage systems (e.g., the Forbach project; Stech et al., 2022), as well as geothermal energy exploitation or seasonal heat storage via the utilization of flooded mine structures (e.g., Loredo et al., 2016; Menéndez et al., 2019). Such developments underscore a growing interest in the sustainable use of the subsurface.

The use of the subsurface can lead to risks related to ground deformation, water management, and induced seismicity (Foulger et al., 2018; Quandt et al., 2023). Consequently, a comprehensive understanding of coupled hydrogeological and geomechanical processes is of both scientific and societal relevance. Globally, mining-related seismicity accounts for approximately 37% of all anthropogenically induced earthquakes (Wilson et al., 2017). In Germany, the societal acceptance of underground activities is particularly sensitive to felt seismicity. In the Saarland coal mining region, for instance, repeated perceptible seismic events have ultimately led to the closure of mines (Alber & Fritschen, 2011; Fritschen, 2010). Numerous studies have been conducted to better understand induced seismicity in mining environments, for example, (Chlebowski & Burtan, 2021; Gibowicz, 2001, 2009; Gibowicz & Lasocki, 2001).

Mining induced seismicity is primarily associated with mass extraction and related processes such as compaction and subsidence, disposal of material (e.g., waste), dewatering, and thermal perturbations (Klose, 2007; McGarr, 1976; McGarr et al., 2002). Most events originate in the immediate vicinity to excavations, where local stress concentrations can lead to rock failure. In the so-called Excavation Damage Zone (EDZ), brittle failure facilitates stress redistribution and partial stress relief (Kelsall et al., 1984). One mechanism contributing to mining induce seismicity is stress arching, a phenomenon of stress redistribution around underground openings. Due to the zero-shear stress boundary condition at the excavation surface, stresses are reoriented and concentrated within the remaining load-bearing structures (Brady & Brown, 2004; Terzaghi, 1943). Therefore, the vertical stress is significantly increased in intact pillars as shown by numerical models (e.g., H. Wang et al., 2013; S. Wang et al., 2013). Esterhuizen et al. (2010) have used numerical modeling to analyze pillar performance in both weak and strong host rocks. Their results demonstrate that pillars may be loaded beyond their peak strength and still maintain structural integrity in stiff rocks or when the span-to-depth ratio is small. In strong rocks, part of the load is transferred to the unmined volumes, whereas for larger span-to-depth ratios and soft rock conditions the full overburden is transferred to pillars. This concept has previously been postulated by Wagner (1974, 1980) and validated by numerical modeling. Huang et al. (2021) have conducted discrete element modeling to investigate stress arching around excavations, focusing on stress concentrations both laterally and above openings in intact and layered rock masses. Most studies on stress arching have primarily addressed the stress state and mechanical strength of mine roofs and pillars (e.g., Huang et al., 2021; Iannacchione et al., 2005; Ning et al., 2022), comparatively few have examined stress concentrations in the immediate floor or beneath excavations (e.g., Lu et al., 2021).

In the post-mining phase, seismic activity typically declines significantly (Arabasz et al., 2005). In many cases, decommissioned mines are allowed to flood to reduce the operational costs of long-term dewatering (Drobniewski et al., 2017). Water flow occurs primarily through open shafts, galleries, and permeable faults zones intersecting the mines. Fluid flow through the rock matrix is comparably slow and therefore of a minor role. The resulting changes in pore pressure alter the effective stresses (McGarr et al., 2002) and could lead to new seismic activity. Lightfoot and Goldbach (1995) have conducted water injection experiments in mines to induce controlled fault slip. In a flooding experiment carried out in an iron mine in Lorraine, Senfaute et al. (2008) have observed a progressive increase in seismicity, which has correlated with the gradual filling of mine voids. In South African gold mines, Goldbach (2009, 2010) has reported a 14-month delay between the onset of flooding and the occurrence of seismic events. Fowkes et al. (2015) have studied flooding-related seismicity in a South African mine, emphasizing the role of frictional slip events on permeable faults and flow through a connected fracture network. Their findings have indicated that a broader range of fault orientations has become prone to slip during flooding. In the former uranium mining area of Schlema-Alberoda, Knoll (2016) has argued that flooding-related seismic events may also occur on faults located farther from previously active mines and with longer time delays, particularly when differential subsidence has been observed and permeable faults are present. Increasing seismicity has also been documented in association with rising water tables during episodes of heavy rainfall (Ogasawara et al., 2002). Dominique et al. (2022) have investigated the relationship between seismicity and

21699356, 2025, 9, Downloaded from https://agupubs.onlinelibrary.wiley.com/doi/10.1029/2025JB031323 by Karlsruher Institut für Technologie, Wiley Online Library on [17/09/2025]. See the Terms and Conditions (https://onlinelibrary.wiley.com/terms-and-conditions) on Wiley Online Library for rules of use; OA articles are governed by the applicable Creative Commons License

groundwater level variations in the abandoned Gardanne coal mine in southern France, where they have observed a delayed seismic response, with some events felt at the surface. Namjesnik (2021) and Yu et al. (2018) have suggested that, over time, mechanical weakening of remnant pillars could lead to induced seismicity on structures close to excavated volumes. An overview of post-mining seismicity has been provided for mines in France, Germany, and Poland as part of the PostMinQuake studies summarized by Contrucci et al. (2023).

The observed delayed seismic responses in some mines suggest a fluid-pressure-driven mechanism. This has been widely interpreted in other subsurface environments, such as geothermal systems, wastewater disposal sites, and CO_2 storage reservoirs, using diffusion models (e.g., Rothert & Shapiro, 2003; Shapiro et al., 2011). These models typically assume that changes in pore pressure propagate through homogeneous, porous, and fully saturated media, governed by Darcy's law and linear poroelasticity (Biot, 1941; Rice & Cleary, 1976; Rothert & Shapiro, 2003; Shapiro et al., 2002). The spatiotemporal evolution of seismicity is often found to correlate with the extent of the pore pressure diffusion front, allowing for predictive modeling of event occurrence based on hydraulic diffusivity. While diffusion-based frameworks have proven effective in many natural geologic settings, its applicability in mining environments remains limited. Mines are typically characterized by strong heterogeneities, discontinuous media, open voids, and sharp permeability contrasts by localized fractured rock mass within the excavation damage zone (EDZ). In such complex settings, pressure transmission may be affected by non-Darcian flow, anisotropic permeability, and discrete fluid pathways forming interconnected networks. In such network-dominated environments, the occurrence of induced seismicity becomes increasingly complex (Goldbach, 2010), and classical diffusion-based models often fail to capture the governing mechanisms, rendering predictions unreliable (Fowkes et al., 2015).

In this study, we investigate seismicity associated with mine water flooding, focusing on the underlying mechanisms and spatial-temporal patterns of induced events. Specifically, we address the following research questions: (a) What are the controlling factors governing the spatial and temporal evolution of seismicity in flooded mining environments? (b) What is the extent and location of mine volumes most susceptible to flooding-induced seismicity?

To address these research questions, high-resolution seismic monitoring data are essential, along with detailed records of mine flooding history, mine geometry, and local and regional stress conditions. The Heinrich-Robert mine is located in the Eastern Ruhr coal mining district. It provides a well-documented case study with comprehensive data. Seismicity in the area has been purely induced. No recent tectonic events have been recorded (Grünthal, 2014; Rische et al., 2023). This has been linked to a low critical stress state in the study area. The stress regime is normal faulting, where the vertical stress (S_V) exceeds the maximum ($S_{H\max}$) and minimum ($S_{h\min}$) horizontal stress (Niederhuber et al., 2025). According to Niederhuber et al. (2025), these gradients are 24.5 MPa/km for $S_{H\max}$, 21.0 MPa/km for S_V, and 15.5 MPa/km for $S_{h\min}$, with $S_{H\max}$ is oriented N134° (Niederhuber, Rische, et al., 2023; Niederhuber, Kruszewski, et al., 2023). Mining activities, however, have been shown to locally perturb the ambient stress field, bringing faults and fractures closer to failure (McGarr et al., 2002). These critically stressed structures can subsequently be reactivated through fluid pressurization, as Hubbert and Rubey (1959) have demonstrated. In this study, we refer to such zones as *volumes of critical stress concentration*.

Seismic monitoring in the Ruhr coal mining area has a long history, beginning in 1908. Since then, observations have been conducted using various regional and temporary local seismic networks (Bischoff et al., 2010; Gibowicz et al., 1990; Mintrop, 1909a, 1909b, 1947; Rische et al., 2023; Wehling-Benatelli et al., 2013). All seismic events recorded by these networks during active mining operations in the Ruhr area have been classified as mining-induced earthquakes, with a maximum observed magnitude of 3.3 M_L (Bischoff et al., 2010). Most events have occurred on steeply dipping fracture planes that strike parallel to the mining face and are of limited spatial extent (Bischoff et al., 2010). There has been no evidence of seismicity occurring along major geological faults (Alber et al., 2009). In the Heinrich-Robert mine, a strong correlation between longwall mining faces and event locations has been observed (Wehling-Benatelli et al., 2013). Induced seismicity has been recorded continuously until mining operations ceased in 2010, followed by a seismic gap that lasted until 2019 (Rische et al., 2023). Flooding began in mid-2019, after which flooding-induced seismicity has been detected. However, these events have also not occurred along major fault structures (Rische et al., 2023). Rische et al. (2023) have indicated that flooding-related seismicity may occur beneath the galleries. However, they have not been able to clearly associate seismicity patterns with features of the mine geometry due to limitations in event localization.

21699356, 2025, 9, Downloaded from https://agupubs.onlinelibrary.wiley.com/doi/10.1029/2025JB031323 by Karlsruher Institut für Technologie, Wiley Online Library on [17/09/2025]. See the Terms and Conditions (https://onlinelibrary.wiley.com/terms-and-conditions) on Wiley Online Library for rules of use; OA articles are governed by the applicable Creative Commons License

21699356, 2025, 9, Downloaded from https://agupubs.onlinelibrary.wiley.com/doi/10.1029/2025JB031323 by Karlsruher Institut für Technologie, Wiley Online Library on [17/09/2025]. See the Terms and Conditions (https://onlinelibrary.wiley.com/terms-and-conditions) on Wiley Online Library for rules of use; OA articles are governed by the applicable Creative Commons License

The precision of event locations has been constrained to approximately 600 m in both horizontal and vertical directions, which is significantly larger than the dimensions of galleries and pillars within the mine.

The aim of this study is to explain the spatial and temporal occurrence of flooding-induced seismicity in a post-mining environment. We use extended seismological time series and perform event relocalization based on updated velocity models. We develop generic three-dimensional geomechanical finite element models of increasing complexity to investigate the influence of various factors, including the elevation and inclination of mined panels and the width of pillars. We focus specifically on the stress and pore pressure distribution in volumes located beneath the mining panels, in depths where seismicity is observed. We further relate our findings to localized microseismicity, mine geometry, and the flooding history of the Heinrich-Robert mine. Our approach incorporates stress-dependent permeability enhancement and poro-mechanical coupling in unsaturated zones, thereby addressing limitations inherent in conventional diffusion-based models.

2. Geological Setting

The Upper Carboniferous strata in the Ruhr area, located in western Germany, is notable for its extensive coal deposits, and their exploitation have historically served as a major driver of regional economic activity. Active coal mining ended in 2018 (Meschede & Warr, 2019). The Ruhr Basin extends about 150 km in NE-SW and about 80 km in NW-SE (Drozdzewski, 1993; Drozdzewski et al., 2009). Sedimentary thicknesses range from 4 km (Meschede & Warr, 2019) to 5.5 km (Alber et al., 2009), and the basin has been structurally overprinted by folding and thrusting associated with the northwestward migration of the Variscan orogeny (Drozdzewski et al., 2009). During the Upper Carboniferous, up to 3.5 km of coal-bearing strata were deposited, consisting of cyclic sequences of sandstones, siltstones, shales, and coal seams (Richter, 1971; Schäfer, 2019; Suess et al., 2007). These folded Carboniferous units are unconformably overlain by Cretaceous marine sediments, which increase in thickness toward the northwest (Drozdzewski, 1993; Richter, 1971). At shaft Heinrich-Robert, the transition between Cretaceous and Carboniferous strata occurs at a depth of approximately 570 m below the surface.

Thrust faults and NW-vergent Variscan folds (Brix et al., 1988) subdivide the basin into NE-SW trending anti- and synclines (Drozdzewski, 1993). Our study area is located within the Hamm Horst structure within the Bochum main syncline. The latter is divided by the Grimberg Saddle (anticline) in a northern and southern Bochum syncline. The horst is laterally bound by the Sutan thrust fault in the WNW and the Scharnhorst thrust fault in the ESE and the Flierich fault and Radbod normal faults in the west and east respectively (Figure 1a). Within the horst only some minor faults are known. Allgaier et al. (2024) has described E-W and N-S trending strike-slip faults in the basement of the Heinrich-Robert mine. Toward the major thrust faults, such as the Sutan fault, the number of minor faults increases (Figure 1b).

3. Heinrich-Robert Mine and Flooding Activities

The Heinrich-Robert mine is part of the "Verbundbergwerk Ost" colliery within the Haus Aden water province. The mine is located on the Hammer Horst, between the Flierich and Radbod faults (Figure 1). Mining in Heinrich-Robert began in 1901 (Voß, 1994) and multiple mining levels have been developed at depths corresponding to economically viable coal seams. The primary mining levels are situated at depths of −890, −970 and −1,120 m (Figure S.5 in Supporting Information S1). The mine has been developed using longwall mining techniques, progressing from NW to SE (Figure S.5 in Supporting Information S1). Coal seams are excavated to increasing depths, following the NE-SW striking fold structures of the basin (Figure 1). The excavation height is determined by the average thickness of the coal seams, which in Heinrich-Robert is approximately 2 m (Figure S.5 in Supporting Information S1), consistent with other German hard coal deposits (Langefeld & Paschedag, 2019).

Prior to the commencement of mining activities, the deep, highly saline and dense groundwater exhibited minimal interaction with the regional flow system. Only in isolated locations, such as brine springs south of the Münsterland, deep groundwater emerges at the surface (ahu AG, 2017). Through mining operations, deep groundwater has been drained from the Upper Carboniferous formations down to depths of approximately −1,400 m. The overlying shallow groundwater remains hydraulically isolated by the impermeable Emscher Marls, effectively preventing direct influence from surface precipitation on mining-related water levels. The Cenomanian and Turonian limestones, situated between the Emscher Marls and the Carboniferous strata, are considered as an aquifer with a broad catchment area and may contribute to groundwater inflow into the mining zones (Hahne

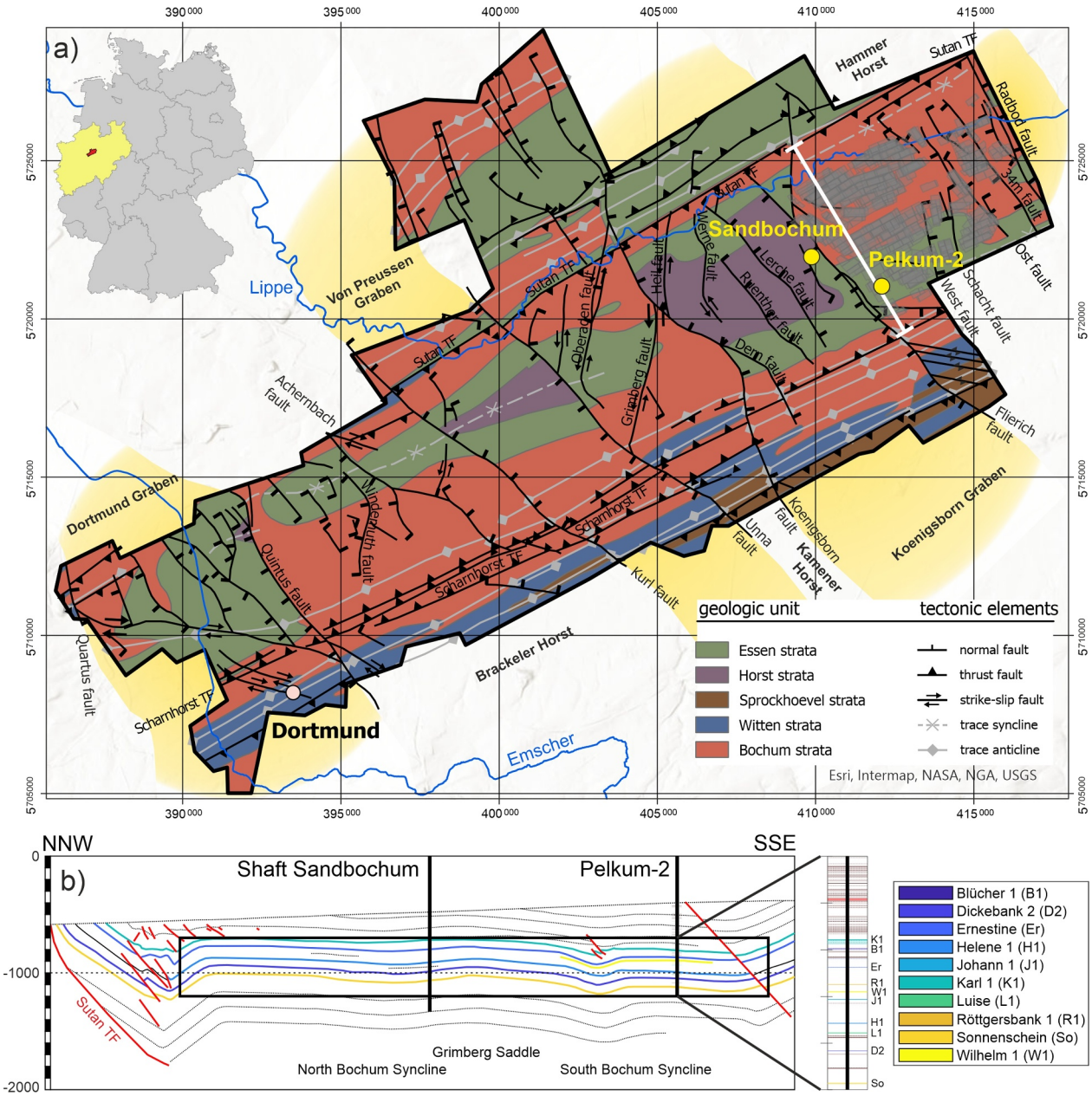

Figure 1. (a) Tectonic map of the Carboniferous surface in the Haus Aden water province, showing major faults and structural features. The map includes parts of the Bochum syncline and minor parts of the Essen syncline, based on Kunz (1988) and Wrede (1988). The location of the Heinrich-Robert mine within the Hammer Horst is marked (based on RAG-BID, 2023) along with the borehole locations (yellow dots). Graben structures are highlighted in yellow. (b) Cross section through the Heinrich-Robert mine based on Kunz et al. (1988) including also minor faults (red) and the approximate extent of Heinrich-Robert mine (black box). Coal seams as well as the enhanced vertical profile of the nearby borehole Pelkum-2 based on GD NRW (1971) are color coded according to Niederhuber et al. (2025). In the profile red lines represent faults, while brown lines are unmined coal seams.

et al., 1982). Consequently, accurately predicting the extent to which precipitation from distant regions influences infiltration into the Upper Carboniferous formations remains a complex and uncertain task.

Faults may act as fluid pathways, as evidenced by observed gas seepages (Thilemann, 2000; Ukelis et al., 2023). However, Rudolph et al. (2010) have reported that the subsurface of the Ruhr area is generally characterized by low permeability and sealing fault structures. Further investigations on rock samples have confirmed that the porosity and permeability of Carboniferous rocks are very low (Greve et al., 2023; Koch et al., 2009). In contrast, mine infrastructure, such as shafts, galleries, and mined panels, constitutes artificial pathways with significantly

21699356, 2025, 9, Downloaded from https://agupubs.onlinelibrary.wiley.com/doi/10.1029/2025JB031323 by Karlsruher Institut für Technologie, Wiley Online Library on [17/09/2025]. See the Terms and Conditions (https://onlinelibrary.wiley.com/terms-and-conditions) on Wiley Online Library for rules of use; OA articles are governed by the applicable Creative Commons License

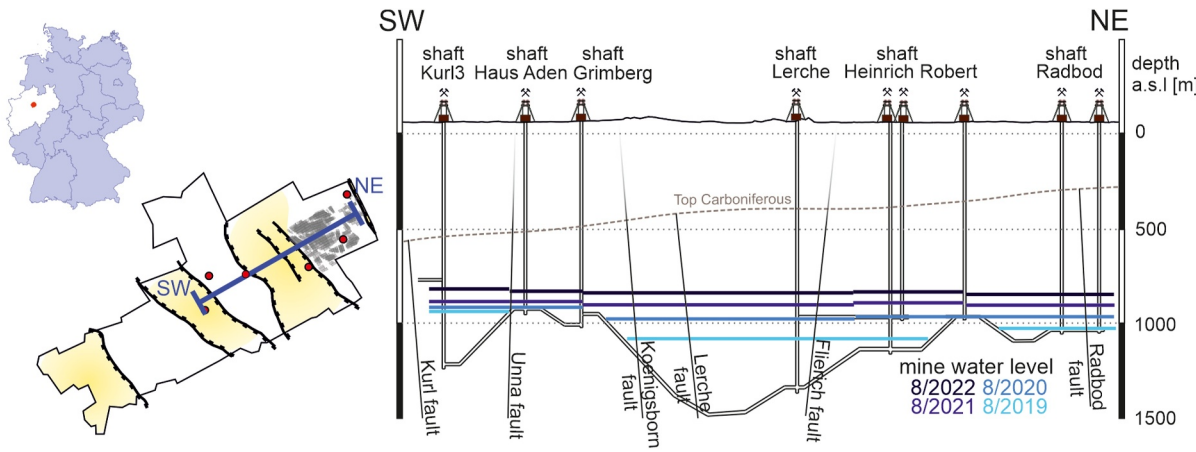

Figure 2. Left: Map of the Haus Aden water province showing monitoring shaft locations (red dots), major faults, and the SW-NE profile line. The shaded gray area marks the extent of the Heinrich-Robert mine; right: Schematic SW-NE cross section of the central dewatering system, illustrating the underground pipe network, monitoring shafts, major faults, and water levels from August 2019 to August 2022, based on Maibaum (2012).

higher permeability (Hahne et al., 1982). These structures facilitate rapid adjustment of water levels within the mine during flooding.

During active mining at the "Verbundbergwerk Ost" colliery, mine water has been managed by lifting all water through the Heinrich-Robert and Haus Aden shafts (Figure 2). In 2013, pumping operations at the Heinrich-Robert shaft ceased, and all mine water has since been lifted at the Haus Aden site (RAG, 2023). In the early stages of mine flooding, water levels rose independently in each mine (Heinrich-Robert, Radbod, Haus Aden, and Monopol) due to isolated hydraulic conditions resulting from differences in mining depths. In mid-2019, pumping operations at the Haus Aden shaft have been discontinued. As the mine water level approached −970 m, hydraulic connectivity between the collieries increased, including connections to adjacent mines such as Radbod and Werne. This expansion of the hydraulic network significantly slowed the rate of water level rise (Figure S.8 in Supporting Information S1). Prior to the establishment of these hydraulic connections, relatively small volumes of water were sufficient to produce noticeable increases in water level. However, following the interconnection of the mine systems, substantially larger volumes of water have been required to achieve comparable rises, due to the increased storage capacity and expanded hydraulic connectivity.

Since 2021, all mines have been hydraulically connected to the Haus Aden shaft, resulting in a more linear increase in water levels. This connection allows water in the entire water province to rise to approximately −600 m (RAG, 2014), but a slight time shift in the water level is currently observed between the shaft Lerche in the SW part of the mine Heinrich-Robert to shaft Sandbochum in the NW part. The latest strategy (DMT, 2023) aims to stabilize the final water level at around −380 m. Once this level is reached, pumping will continue to prevent mixing of deep saline water with shallow freshwater. Extensive areas of the Ruhr region have experienced subsidence exceeding 25 m due to historical mining activities (Harnischmacher, 2010), making continued pumping also essential to avoid flooding.

4. Seismological Database and Data Processing

We use data from a temporary network of up to 32 short-period seismological sensors focused on the Heinrich-Robert mine (Figure 3a), as previously described by Friederich et al. (2020) and Rische et al. (2023), along with data from the RuhrNet operated by Ruhr University Bochum (2007). We expand the analysis of Rische et al. (2023) for the time series from 6/2019 until 6/2024. Seismic events are identified using automatic detection algorithms, including STA/LTA and cross-correlation triggers, as well as through manual inspection of waveform data. Visual inspection allows us to detect small events in previously inactive areas, even in the absence of waveform templates, which are often missed by automated systems (Rische et al., 2023). We manually pick arrival times of Pg and Sg phases, and, where possible, determine the polarities of first arrivals. Automatic picks are reviewed and corrected to ensure accuracy.

21699356, 2025, 9, Downloaded from https://agupubs.onlinelibrary.wiley.com/doi/10.1029/2025JB031323 by Karlsruher Institut für Technologie, Wiley Online Library on [17/09/2025]. See the Terms and Conditions (https://onlinelibrary.wiley.com/terms-and-conditions) on Wiley Online Library for rules of use; OA articles are governed by the applicable Creative Commons License

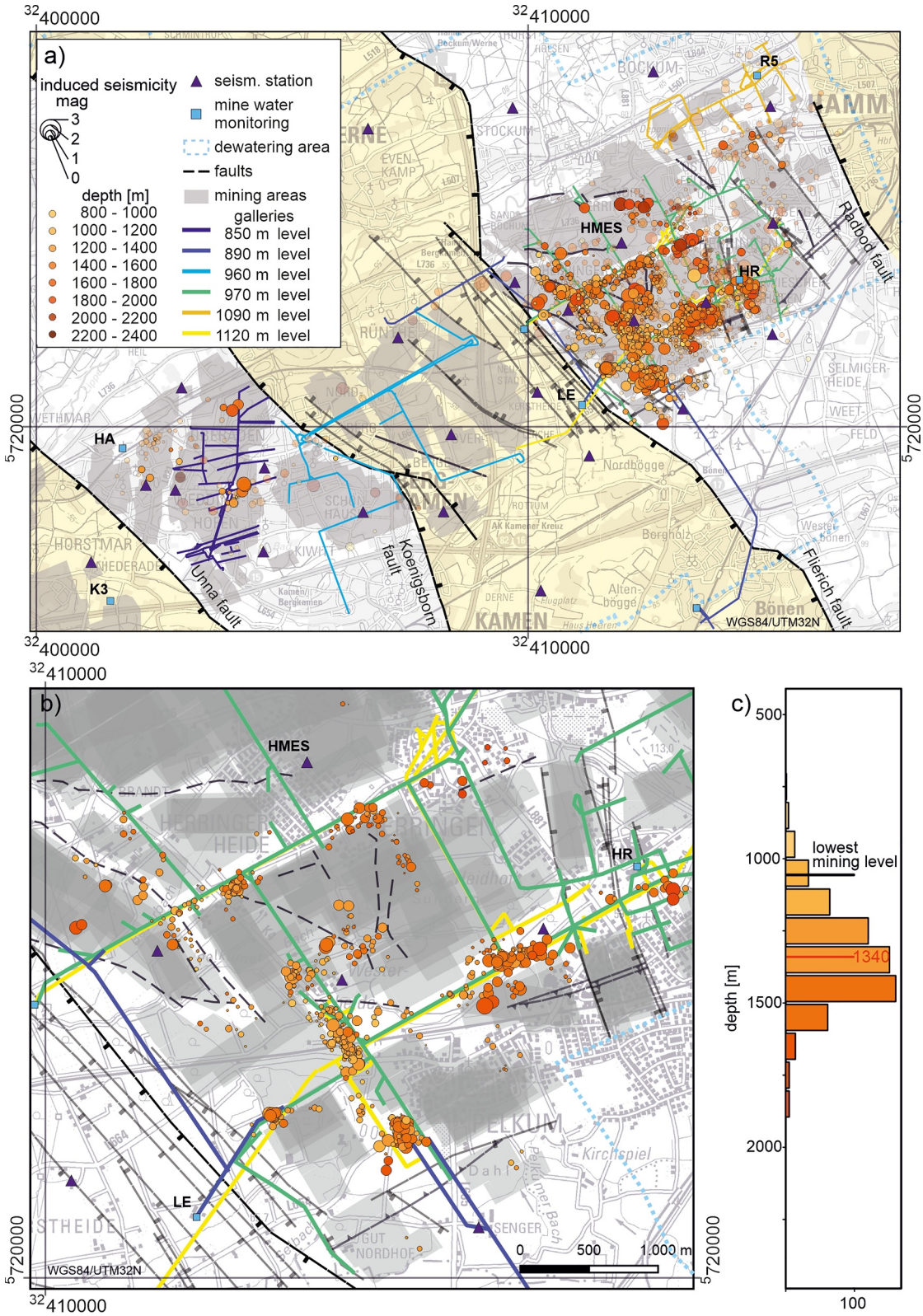

Figure 3.

21699356, 2025, 9, Downloaded from https://agupubs.onlinelibrary.wiley.com/doi/10.1029/2025JB031323 by Karlsruher Institut für Technologie, Wiley Online Library on [17/09/2025]. See the Terms and Conditions (https://onlinelibrary.wiley.com/terms-and-conditions) on Wiley Online Library for rules of use; OA articles are governed by the applicable Creative Commons License

By default, we localize all seismic events using the NonLinLoc algorithm (Lomax et al., 2000, 2009) integrated within the SeisComP package (Helmholtz Centre Potsdam GFZ, 2008) and perform magnitude determination for each event. For single-event localization, we apply a layered 1D velocity model adapted from a regional crustal model that has been used in Rische et al. (2023), incorporating depth steps at 4, 12, 22, and 32 km, with a constant *Vp*/*Vs* ratio of 1.73 (orange line in Figure S.3.1h in Supporting Information S1). For relative relocalization of seismic events, we apply the double-difference method using hypoDD, according to Waldhauser and Ellsworth (2000). In our study, we use a search distance of 150 m within the single-linkage clustering algorithm and use the catalog differential times to relocate the clusters (parameters in Supplement 3, Table S.3.1 in Supporting Information S1). Although the double-difference technique reduces sensitivity to the velocity model, we test multiple models to assess its influence (Figure S.3.1 in Supporting Information S1).

5. Distribution of Microseismicity

We compile an event database comprising approximately 2,500 induced seismic events with local magnitudes ranging from −0.9 to 2.6 M_L and a magnitude of completeness exceeding 0.3 M_L. The magnitude distribution (Figure S.9 in Supporting Information S1) indicates a deficit of events with magnitudes greater than $M_L = 2$. Using single-event localization, we localize seismic events at depths between −800 and −2,400 m. For approximately 930 events, the spatial uncertainty remains below 600 m (Figure 3a), and for about 630 events, we achieve a localization better than 100 m (Figure 3b). Notably, nearby large-scale (kilometer-scale) faults show no increase in seismic activity, confirming the initial findings reported by Rische et al. (2023).

This study refines the seismicity distribution using relatively localized hypocenters (Figure 3b). Despite the smaller number of relocalized events, the overall spatial distribution, including clustering beneath the galleries, remains consistent (compare Figures 3a and 3b). Also, the event depth, which is a key focus in our study shows a consistent peak distribution between −1,200 and −1,600 m (Figure S.6 in Supporting Information S1, Figure 3c) for all tested velocity models. When we use the model with the best trade-off between RMS values and data loss ($v_{P_up} = 3$ km/s), relocated events concentrate between −1,200 and −1,500 m, with a mean depth of −1,340 m (Figure 3c), clustering vertically 200–500 m below the mining level. Horizontally, events cluster around remnant pillars between the mined panels (Figure 3b). Fault plane solutions from 30 events indicate steeply dipping faults. However, they show no depth-dependent or temporal clustering of mechanism types (Supplement 4 in Supporting Information S1), suggesting that seismicity is primarily controlled by local stress redistribution rather than regional tectonic stress regimes.

6. Numerical Model

To investigate the factors controlling flooding-induced seismicity, we develop three generic finite element model geometries based on a simplified mine geometry consisting of four panels (Figure 4). We progressively increase the complexity of the models by varying the depth and curvature of the mine panels, and the pillar width (see following sections for material properties, physics, boundary conditions and model set-up). For one of the generic configurations, we compare the results of a static versus a transient approach and assess the influence of different ambient stress states. Additionally, we evaluate the impact of stress dependent permeability enhancement. Unlike real mine geometries, where multiple interacting factors may obscure individual effects, the generic models enable a controlled examination of specific influences on induced seismicity during flooding. Finally, we compute a static model using the actual mine geometry of Heinrich-Robert mine (Figure 5) and compare clusters of critically stressed volumes with observed induced seismicity.

Figure 3. (a) Induced seismicity from 6/2019 until 6/2024 in the former "Verbundbergwerk Ost" colliery. Approximately 2,500 events are localized (transparent colors), of which ∼930 exhibit spatial uncertainties <600 m (solid colors). Gray shaded areas represent projections of all mining levels, ranging from −725 m to −1,150 m; (b) Distribution of 631 relocated events with spatial uncertainties <100 m. White areas between mined panels indicate remnant pillars, which also host the galleries (colored lines). Most events occur beneath the lowest galleries. Gray transparent polygons denote mined panels at various depths (as projected in panel a), indicating that some pillars span multiple levels or are undermined; (c) Depth distribution of relocated events, with a peak between −1,200 and −1,500 m. The mean event depth is −1,340 m, approximately 370 m below the main mining level.

21699356, 2025, 9, Downloaded from https://agupubs.onlinelibrary.wiley.com/doi/10.1029/2025JB031323 by Karlsruher Institut für Technologie, Wiley Online Library on [17/09/2025]. See the Terms and Conditions (https://onlinelibrary.wiley.com/terms-and-conditions) on Wiley Online Library for rules of use; OA articles are governed by the applicable Creative Commons License

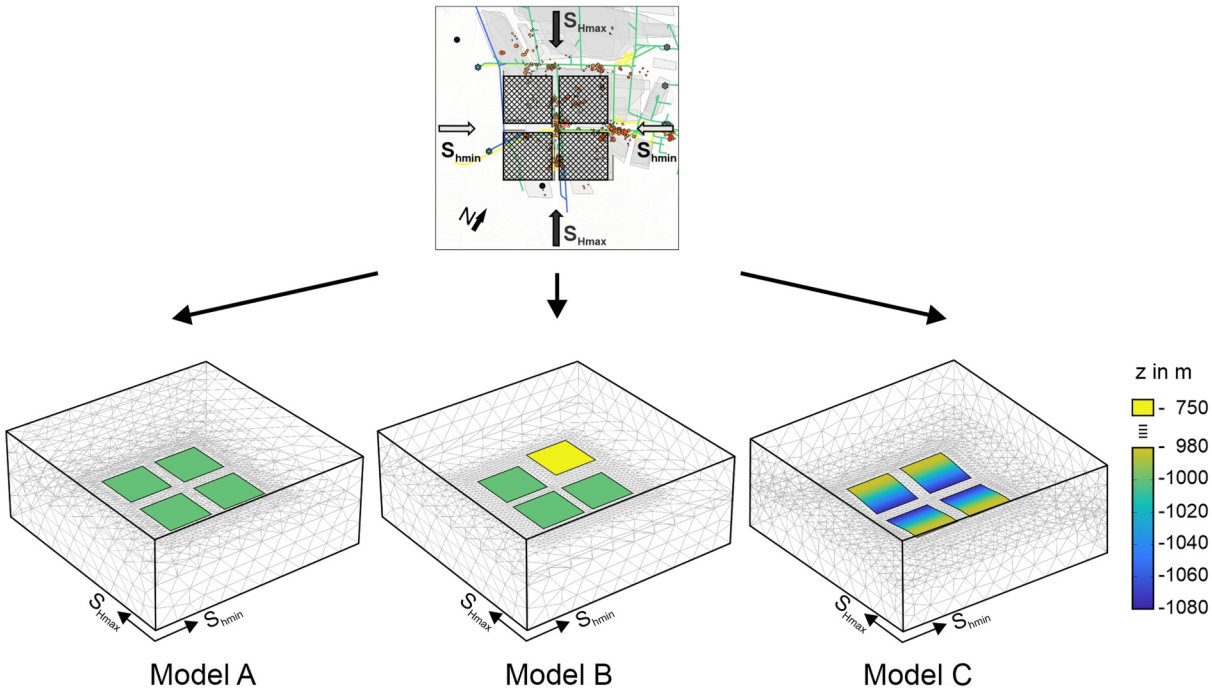

Figure 4. Generic mine models used for numerical simulations, simplified to four mined panels. Model A includes four panels at a uniform depth of −1,000 m. Model B consists of three panels at −1,000 m and one at −750 m. Model C reflects the simplified morphology of coal seams. All model boundaries are aligned with principal stress orientations. Each model is subdivided into mesh domains, with finer resolution in the inner domains and coarser mesh in the outer regions.

6.1. Rheology and Physics

Hydraulic fracturing stress measurements within the Heinrich-Robert mine have not shown lithology-dependent variations (Niederhuber et al., 2025). Consequently, the models assume a homogeneous subsurface material. This simplification reduces geometric complexity and avoids high aspect ratios in mesh elements, thereby enhancing numerical stability and improving convergence. The parameters applied in the simulations are summarized in Table S.4 of Supporting Information S1.

Stress redistribution near excavations can lead to rock failure. We consider two failure modes and the influence of pore pressure P_p, assuming compressive stress as positive and tensile stress as negative. The effective stress is coupled with pore pressure changes using the linear poroelasticity law (Equation 1):

$$\sigma_{ij} = S_{ij} - \alpha P_p \delta_{ij} \tag{1}$$

where σ'_{ij} is the effective stress, S_{ij} the total stress tensor, α is the Biot's coefficient, and δ_{ij} is the Kronecker delta (1 if $i = j$ and 0 if $i \neq j$). Tensile failure occurs when the effective minimum principal stress σ_3 is smaller than the tensile strength T of the rock (Equation 2):

$$\sigma_3 < T \tag{2}$$

Compressive failure occurs if the shear stress τ exceeds the failure envelope (linear Mohr Coulomb criterion for 2D as shown in Figure S.7.1 in Supporting Information S1 or Tresca criterion for 3D, respectively). The failure envelope is defined by the effective normal stress σ_N, the pore pressure P_P, coefficient of static friction μ and the cohesion C_0 (Equation 3):

$$\tau > \mu \cdot \sigma_N + C_0 \tag{3}$$

Cohesion C_0 is calculated based on the uniaxial compressive strength UCS and the coefficient of friction μ using Equation 4 based on Jaeger et al. (2007):

21699356, 2025, 9, Downloaded from https://agupubs.onlinelibrary.wiley.com/doi/10.1029/2025JB031323 by Karlsruher Institut für Technologie, Wiley Online Library on [17/09/2025]. See the Terms and Conditions (https://onlinelibrary.wiley.com/terms-and-conditions) on Wiley Online Library for rules of use; OA articles are governed by the applicable Creative Commons License

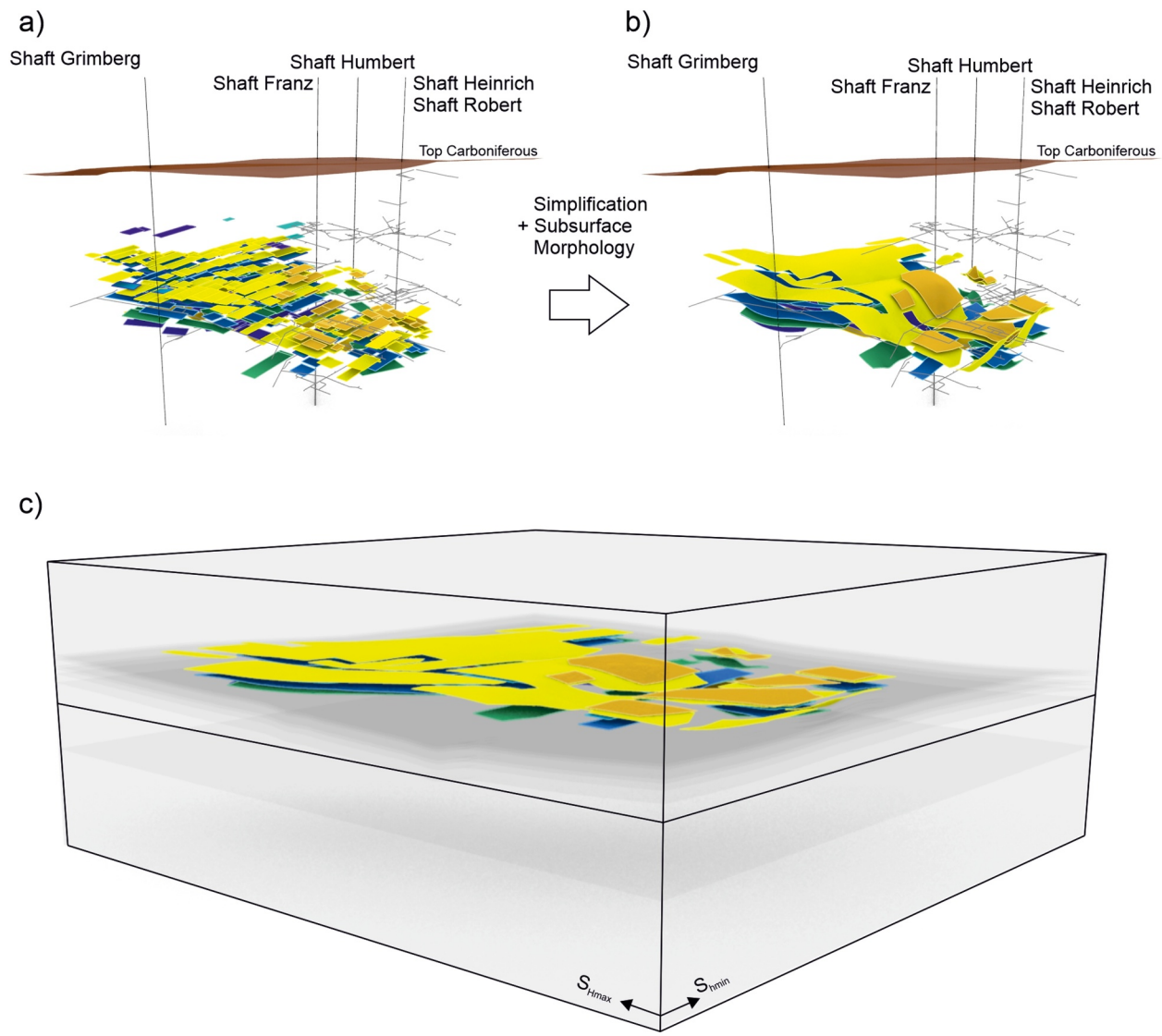

Figure 5. (a) Mined panel surfaces in the study area, provided by RAG-BID (vertical exaggeration by a factor of 5). (b) Smoothed surfaces of mined panels based on depth variations of the coal seams (workflow shown in Figure S.4 in Supporting Information S1). (c) In model D the smoothed surfaces are embedded within a model cube oriented parallel to the principal stress orientations, consistent with models A–C.

$$C_0 = UCS\frac{1 - \sin\varphi}{2\cos\varphi} \tag{4}$$

For Ruhr sandstone, we establish a friction coefficient of $\mu = 0.60$, consistent with values reported by Byerlee (1978). Alber and Schwarz (2015) have identified this value as an upper bound for weakly coal-coated fractures, and Duda (2011) has reported friction coefficients ranging from 0.6 to 0.7 derived by triaxial test of Ruhr Sandstone.

The maximum shear stress $\tau_{\max}$ where resistant forces (normal effective stress and cohesion) are in equilibrium with the driving forces (shear stress) is defined as maximum shear capacity $\tau_{\max}$, based on the Mohr Coulomb criterion (Equation 5):

$$\tau_{\max} = \sin(\varphi)\cdot\frac{\sigma_1 + \sigma_3}{2} + C_0 \tag{5}$$

21699356, 2025, 9, Downloaded from https://agupubs.onlinelibrary.wiley.com/doi/10.1029/2025JB031323 by Karlsruher Institut für Technologie, Wiley Online Library on [17/09/2025]. See the Terms and Conditions (https://onlinelibrary.wiley.com/terms-and-conditions) on Wiley Online Library for rules of use; OA articles are governed by the applicable Creative Commons License

The equation can be rewritten in the form of the proximity of the state of stress to the failure envelope, or distance of Mohr Circle to Failure Envelope (*DMF*). Thereby the radius of the Mohr Circle defined by the minimum and maximum principal effective stress is subtracted from the maximum shear capacity (Equation 6):

$$DMF = \sin(\varphi) \cdot \frac{\sigma_1 + \sigma_3}{2} - \frac{(\sigma_1 - \sigma_{3)}}{2} + \left[C_0 \cdot \frac{\sin(\operatorname{atan}(\mu))}{\mu} \right] \tag{6}$$

For both failure mechanisms, a stress-weakening approach is introduced, where the stresses in the volumes matching the failure criteria are completely relieved, as is common in fractured rocks (Brady & Brown, 2004).

For failure, the effective stresses and thus the pore pressure (Equations 2 and 3) must be considered. The spatial and temporal distribution of pore pressure depends on permeability. The Upper Cretaceous Ruhr Sandstone is characterized by low intrinsic permeability, with fluid flow predominantly controlled by fracture permeability (Allgaier et al., 2023; Creutzberg, 1963; Greve et al., 2023; Jagert et al., 2023; Kück, 1988). Stress concentrations near mines, particularly in pillars, may alter the intrinsic permeability k_{int}. While elevated stress generally reduces permeability by closing microfractures (Bohnsack et al., 2021; Durucan & Edwards, 1986; Song & Elsworth, 2024; Zheng et al., 2015), the effect is minor and not considered in the model. In contrast, permeability can increase by several orders of magnitude due to fracture formation or shear dilation (Durucan & Edwards, 1986; H. Wang et al., 2013; S. Wang et al., 2013). This increase typically ranges from 10^3 to 10^4 (S. Wang et al., 2013), depending on rock type. Newly formed pathways and fracture networks may vertically extend several hundred meters, depending on the mine geometry (Yin et al., 2016).

Fracture networks can be represented explicitly via discrete fracture models or implicitly through effective continuum approaches (Hörl & Rohde, 2024). To reduce computational cost and avoid detailed fracture data, we adopt an implicit equivalent permeability approach. This modifies the permeability of fractured rock masses (Liu et al., 2016), enabling large-scale flow modeling using Darcy's law (Azizmohammadi & Matthäi, 2017). To account for stress-induced permeability enhancement k_{DMF}, we define a scaling relationship that adjusts the intrinsic permeability k_{int} by a scale factor k_{Sc} (Equation 7):

$$k_{DMF} = k_{\text{int}} \cdot k_{Sc} \tag{7}$$

S. Wang et al. (2013) have observed a moderate permeability increase as fractures approach yield stress, followed by a sharp rise at higher stress or strain levels. We define the scale factor k_{Sc} as an exponential ramp function, dependent on the maximum shear capacity $\tau_{\max}$ and the *DMF* value. A threshold of 0.1 is applied to the *DMF* normalized by $\tau_{\max}$, and the maximum permeability enhancement is capped at 10^4 (Equation 8):

$$k_{Sc} = \begin{cases} 1, & DMF \geq 0 \\ \left(10^4\right)^{\frac{DMF - \tau_{\max}}{\tau_{\max}}}, & DMF < 0\,; \dfrac{DMF}{\tau_{\max}} < 0.1 \\ 10^4, & DMF < 0\,; \dfrac{DMF}{\tau_{\max}} \geq 0.1 \end{cases} \tag{8}$$

Locally unsaturated zones near excavations may violate Darcy's law, resulting in unrealistic negative pore pressures that artificially increase total stress. This issue is often disregarded in numerical models (Abdi et al., 2010; Chen et al., 2019; COMSOL Multiphysics, 2021). To suppress these effects, we implement two measures: (a) Darcy velocities are zero in unsaturated regions, and (b) pore pressure-dependent variables (absolute pressure, hydraulic head, and pressure head) are set to zero. In addition, the poroelastic coupling is disabled in this region by modifying the Biot coefficient α based on pore pressure: $\alpha = 1$ for $P_p \geq 0$, and $\alpha = 0$ for $P_p < 0$.

6.2. Reactivated Volumes and Preferential Fracture Orientations Based on DMF Analysis

The model predicts (a) the spatio-temporal occurrence and magnitudes of stress concentrations, and (b) the locations and orientations of fractures with potential for reactivation using Equation 6. As the reactivation of preexisting faults or fractures is more likely than the formation of new fractures, the cohesion C_0 is set zero. Negative *DMF* values indicate a high likelihood of reactivation, while positive values suggest stability. The volume with negative *DMF*, denoted V_{DMF}, serves as a proxy for fault reactivation and is computed at each time step using a piecewise Heaviside function. Analogue to Shapiro et al. (2010) we use a statistically homogeneous set of fractures within the medium. Higher V_{DMF} values indicate increased potential for fracture reactivation.

21699356, 2025, 9, Downloaded from https://agupubs.onlinelibrary.wiley.com/doi/10.1029/2025JB031323 by Karlsruher Institut für Technologie, Wiley Online Library on [17/09/2025]. See the Terms and Conditions (https://onlinelibrary.wiley.com/terms-and-conditions) on Wiley Online Library for rules of use; OA articles are governed by the applicable Creative Commons License

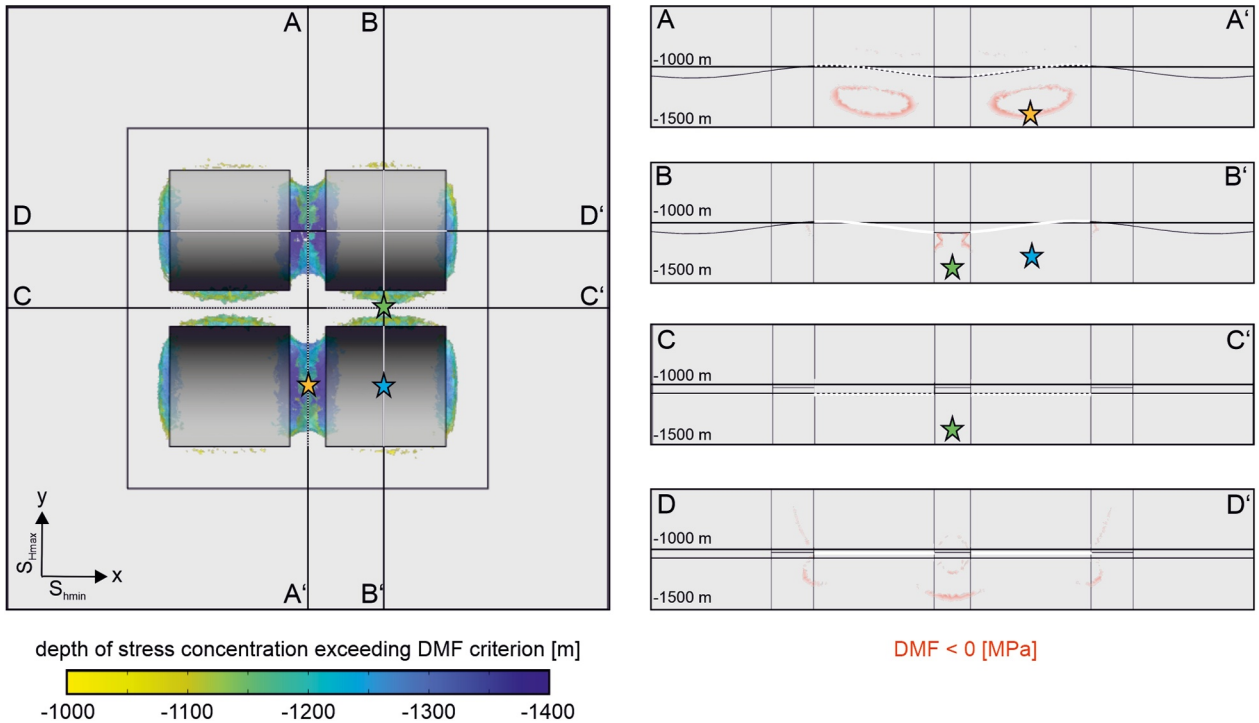

Figure 6. Modeling results of model C for 3,150 days of flooding. Left: Depth where the stress state reaches the failure envelope ($DMF < 0$). Right: Transects showing zones where *DMF* criterion is met. White sectors indicate the positions of mined-out panels within the transects. (Note: The inner box corresponds to the refined mesh domain). In transects C and D the closest of the (inclined) mined panels is projected. Star symbols refer to locations shown in Figure 7.

Additionally, we analyze the fracture orientation associated with the most negative *DMF*. The corresponding orientation is determined by the angle β between the principal stress direction $S1$ and the fault normal vector $\overrightarrow{n_F}$. Details on the 3D calculation of $\overrightarrow{n_F}$ are provided in Supplement 7.

6.3. Setup of the Generic Mine Model

In the Heinrich-Robert mine, galleries are nearly orthogonal, with NNW-oriented galleries aligned with $S_{H\max}$ (Niederhuber, Kruszewski, et al., 2023; Niederhuber, Rische, et al., 2023). Mined panels are represented as 2 m-thick polygons, reflecting the average mining height (Supplement 1 in Supporting Information S1). We tested the influence of galleries, simplified as straight tunnels, on stress redistribution (Supplement 9 in Supporting Information S1). Their effect is highly localized and alters stress only between mined panels. However, as all stress components ($S_{H\max}$, $S_{h\min}$, and S_V) increase (Figure S.11 in Supporting Information S1), the *DMF* values remain below critical. Thus, our generic mine model includes pillar sections but excludes galleries. In model A, all four mining panels are placed at a uniform depth of −1,000 m, with 300 m wide pillars (Figure 4). Model B shifts the northeastern panel to −750 m to reflect varying mining levels in Heinrich-Robert and reduces pillar width to 200 m. Model C introduces subsurface morphology to represent coal seam depth variations, as described in Supplement 1 in Supporting Information S1. The same panel layout as in model A is mapped onto a generic surface (Figure 4) adapted to the Northern and Southern Bochum Syncline (Figure 1).

In model D, we reconstructed the coal seam morphology based on the mining depth of the individual panels and borehole data from Pelkum-2 (details in Supplement 1 in Supporting Information S1). Next, we simplified the geometry of mining panels of each level and mapped them onto the coal seams (Figure 5).

All generic mine models are embedded in a homogeneous volume of 5 × 5 × 2 km, optimized to minimize boundary effects in hydro-mechanical simulations. Model size is iteratively reduced through multi-step fitting to enhance computational efficiency. Geometry generation, meshing, and numerical simulations are performed using COMSOL Multiphysics®. Mesh density is adapted to geometric complexity and local solution requirements via multiple mesh domains. To avoid artificial shear stress at model boundaries during pre-stressing, the model is rotated so that boundaries align with the principal stress orientations (Figure 6).

21699356, 2025, 9, Downloaded from https://agupubs.onlinelibrary.wiley.com/doi/10.1029/2025JB031323 by Karlsruher Institut für Technologie, Wiley Online Library on [17/09/2025]. See the Terms and Conditions (https://onlinelibrary.wiley.com/terms-and-conditions) on Wiley Online Library for rules of use; OA articles are governed by the applicable Creative Commons License

6.4. Boundary Conditions and Initial Values

In the poroelastic model, both solid mechanics and fluid flow require boundary and initial conditions. Roller boundary conditions are applied to vertical sides and the bottom, restricting boundary-normal displacement while allowing in-plane motion. Gravity is imposed as a vertical body force across the domain. To represent pre-flooding conditions, initial stresses are defined as linear gradients: S_V: 24.5 MPa/km, $S_{H\max}$: 21.0 MPa/km, $S_{h\min}$: 15.5 MPa/km (Niederhuber et al., 2025). These gradients are used in the static prestressing step followed by another static step where mechanical equilibrium is established. This state is evaluated using the *DMF* (Equation 6), and the derived *DMF* values are used to calculate the equivalent permeability (Equations 7 and 8), which is employed in subsequent model steps.

We perform transient simulations for models A, B, and C, covering the flooding period from 1 October 2019 (−1,123.7 m), to 12 June 2024 (−738.5 m). For models B and D, we conduct static simulations based on the final flooding level of −600 m. In the transient models, equivalent permeability is updated at each time step. Hydraulic conditions are initialized using a hydraulic head, resulting in a hydrostatic pore pressure gradient. Zero pore pressure boundaries are applied at the mined panels. A static solution yields the equilibrium pore pressure distribution with reduced pore pressures in the vicinity of the mine.

To simulate mine water rise, pore pressure on the mined panels is increased over time based on water level data from RAG AG (RAG-BID, 2023). These shaft recordings, referenced to sea level, are linearly interpolated to define the function $WL_{\text{int}}(t)$. At each time step, the mining depth z (also relative to sea level) is compared to $WL_{\text{int}}(t)$. If $WL_{\text{int}}(t) \leq z$, no pore pressure is applied. If $WL_{\text{int}}(t) > z$, pore pressure is computed by integrating fluid density over the height difference $WL_{\text{int}}(t)$—z.

This approach reproduces the findings of Hahne et al. (1982), who have shown that in mines with Emscher Marl stratigraphically overlying the Carboniferous, water inflow originates from the Cenomanian rocks (Figure S.5 in Supporting Information S1). Infiltrating water is first intercepted by the uppermost lateral mining level and then transported via shafts and galleries to deeper levels. As a result, the upper mine sections are drained while lower sections are progressively flooded, depending on the mine water level. Due to the large diameters of shafts and galleries, fluid velocities are higher, and thus pressure changes occur significantly faster than in porous media. Lateral flow contributions are represented by hydrostatic far-field conditions, as demonstrated by Niederhuber et al. (2025).

In addition to the transient model, which simulates time-dependent water level changes, we develop a static model to represent the final flooding phase, where stress and pore pressure have reached equilibrium. Boundary conditions match those of the transient case, except for a fixed water level at −600 m. The spatial extent of fault and fracture reactivation is derived from the distribution of negative *DMF*. Unlike the retrospective transient models, the steady-state model offers predictive capability.

7. Results of Numerical Modeling

The transient models (A, B, C) simulate flooding from 2019 to 2024 up to a water level of −738 m. In addition, we performed a static simulation for model B, while model D represents purely static conditions. Since most flooding-induced seismicity has occurred approximately 300 m below the lowest mining level, concentrated beneath pillars between panels (Figures 3b and 3c), we focus our analysis on model results at this depth.

7.1. Model A—4 Panels at −1,000 m

At the final time step of the transient model (12 June 2024), *DMF* values indicate elevated reactivation potential, particularly beneath pillars between mined panels. Reactivation is most pronounced in $S_{H\max}$ -aligned pillars, with failure depths reaching −1,200 to −1,400 m, while $S_{h\min}$ -aligned pillars exhibit shallower failure. This underscores the influence of stress orientation on failure depth (Supplement 8 in Supporting Information S1).

7.2. Model B—3 Panels at −1,000 m, One at −750 m

Model B includes two scenarios: (a) transient flooding with a time-dependent water level (Figure S.13 in Supporting Information S1), and (b) a static simulation representing the final flooding state with pore pressure equilibrium (Figures S.14 and S.15 in Supporting Information S1). Additionally, we tested the impact of different

21699356, 2025, 9, Downloaded from https://agupubs.onlinelibrary.wiley.com/doi/10.1029/2025JB031323 by Karlsruher Institut für Technologie, Wiley Online Library on [17/09/2025]. See the Terms and Conditions (https://onlinelibrary.wiley.com/terms-and-conditions) on Wiley Online Library for rules of use; OA articles are governed by the applicable Creative Commons License

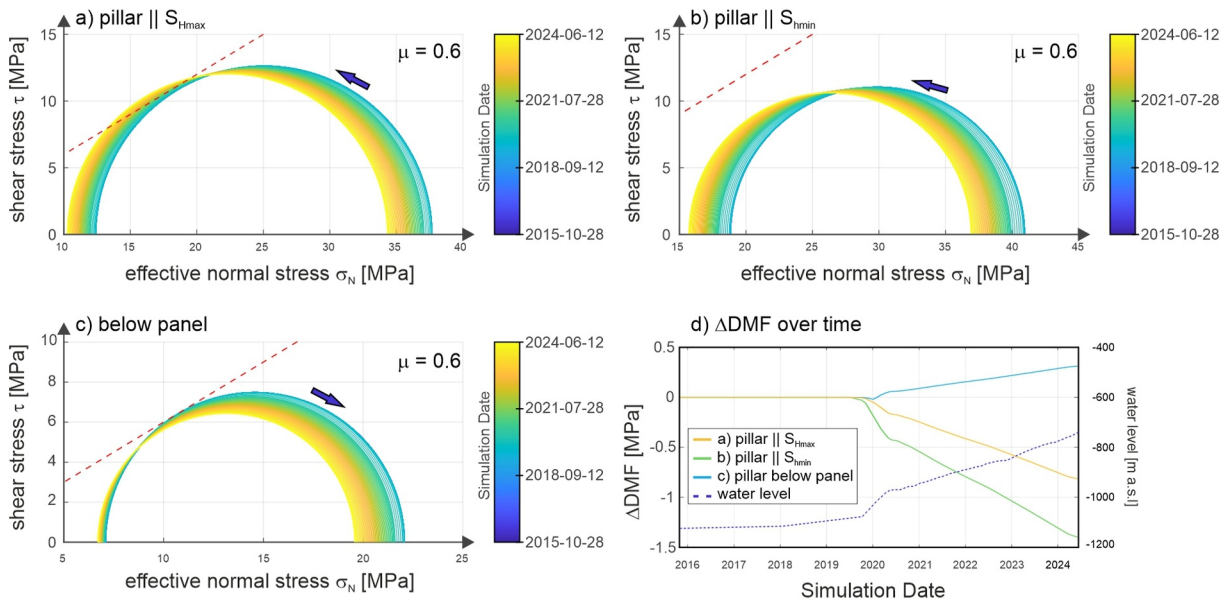

Figure 7. Mohr circle diagrams for model locations marked with stars in Figure 6. Colors indicate the date of flooding. Arrows pointing toward the failure envelope indicate decreasing DMF with progressive flooding, while arrows pointing away suggest increasing *DMF*. (a, b) Within pillars aligned with $S_{H\max}$ or $S_{h\min}$, increasing pore pressure reduces effective stress of *S*1 and *S*3. (c) Beneath mined panels, *S*3 is nearly unaffected by increasing pore pressures and Mohr circles decrease in size with time. (d) Temporal evolution of ΔDMF and water level (Note: *x*-axis does not start at zero for improved visibility).

stress regimes on the modeling results with the static model (Figure S.16 in Supporting Information S1). The shallower panel in the upper right modifies the stress field, producing a broader and more asymmetric distribution of negative *DMF* compared to model A. In areas unaffected by panel elevation, reduced pillar width (200 vs. 300 m) leads to more extensive negative *DMF* zones, particularly in $S_{h\min}$ -aligned pillars. Compared to $S_{H\max}$ -oriented pillars, failure zones in $S_{h\min}$ -aligned pillars extend more broadly between mined panels, as shown in Figures S.11 and S.13 in Supporting Information S1. The static simulation with a fixed water level of −738 m reproduces the spatial pattern of negative *DMF* observed in the transient case (Figure S.14 in Supporting Information S1). Mohr circle analysis reveals elevated vertical stress within and beneath pillars, indicating a high likelihood of shear failure under increasing pore pressure (Figure S.15 in Supporting Information S1). A comparison of stress regimes—normal faulting (Niederhuber et al., 2025) and strike-slip (Kruszewski et al., 2022)—shows similar reactivation patterns (Figure S.16 in Supporting Information S1).

7.3. Model C—Four Curved Panels

In model C, zones of negative *DMF* values peak in the pillar aligned with $S_{H\max}$ (Figure 6). The depth distribution of these zones is strongly influenced by coal seam morphology and the geometry of mined panels. While the elliptical shape of the *DMF* zones remains consistent with previous models (Figures S.11 and S.13 in Supporting Information S1), the major axis now aligns with morphological features (transect A-A′, Figure 6). In the $S_{h\min}$ aligned pillar (transect C-C′) adjacent panel morphology intensifies negative *DMF* compared to model A with flat panels. Along transect D-D' (parallel to syncline and $S_{h\min}$), morphological effects are minimal and *DMF* resemble those in model A.

Water level changes during flooding are highly heterogeneous in space and time. Three representative locations are shown in Figure 8, with Mohr circles (representing the 2D stress state) plotted for each time step (30 days) between 1 October 2019, and 12 June 2024. Beneath pillars, increasing pore pressure shifts Mohr circles toward lower effective stresses, leading to failure (Figures 7a and 7b). Changes are more pronounced in $S_{h\min}$ -aligned pillars (Figure 7b) compared to $S_{H\max}$ -aligned pillars (Figure 7a)). The first are closer to mined panels due to the coal seam morphology, resulting in faster pore pressure rise and decreasing ΔDMF (Figure 7d). Beneath panels, vertical stress (S_V) decreases, transitioning the stress regime to thrust faulting ($S_V = S3$). At position c) the state of stress gets less critical during flooding because rising water increases vertical stress, reducing the Mohr circle

21699356, 2025, 9, Downloaded from https://agupubs.onlinelibrary.wiley.com/doi/10.1029/2025JB031323 by Karlsruher Institut für Technologie, Wiley Online Library on [17/09/2025]. See the Terms and Conditions (https://onlinelibrary.wiley.com/terms-and-conditions) on Wiley Online Library for rules of use; OA articles are governed by the applicable Creative Commons License

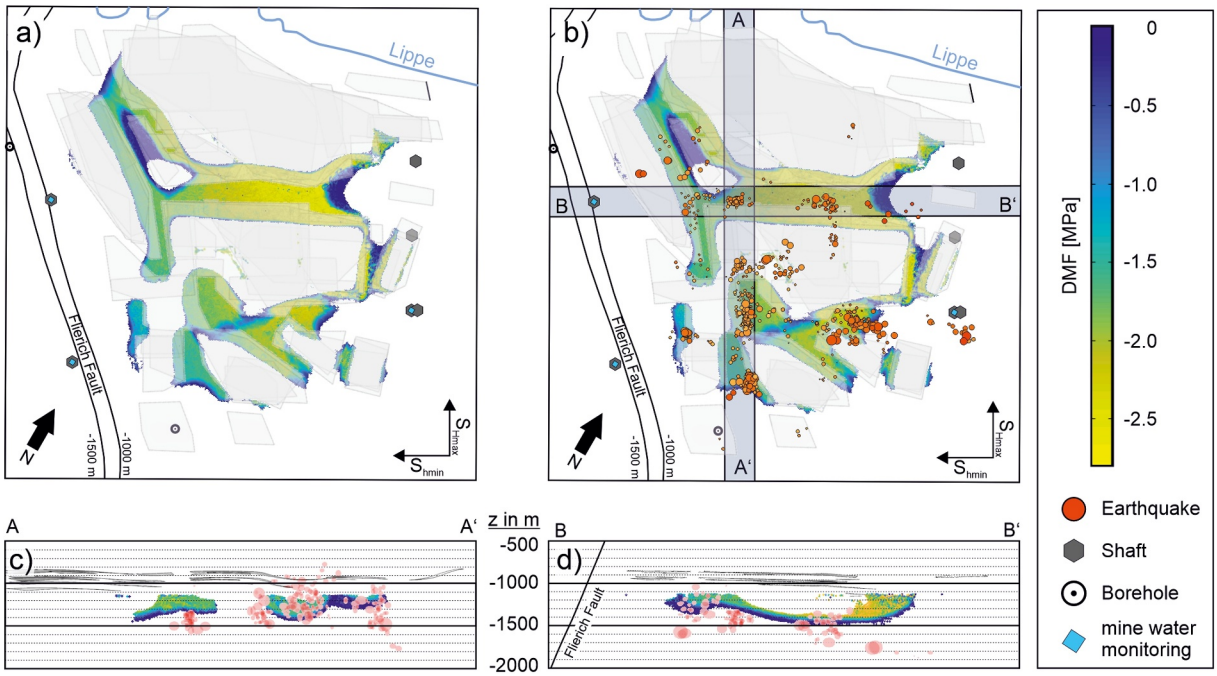

Figure 8. Results of the *DMF* analysis for model D. (a) Projected *DMF* values in map view. (b) Overlay of the map view with relocalized earthquake locations (from Figure 3b) and traces of the transects used for (c, d). (c) Transect parallel to $S_{H\max}$ showing *DMF* values along with relocated earthquake locations. (d) transect parallel to $S_{h\min}$ showing *DMF* values along with relocated events. Symbol sizes in panels (c, d) reflect location uncertainties in *x*, *y*, and *z* directions.

radius and counteracting pore pressure effects (Figure 7c). Horizontal stress changes are minor and governed by the Poisson's ratio. The smaller radius indicates greater stability, with increasing ΔDMF (Figure 7d).

7.4. Model D—Real Mine Geometry

In static model D, pore pressure is analytically added to modeled total stress to represent effective stress during flooding. Negative *DMF* concentrates within pillars (Figure 8a). The depth of these zones depends on the number and depth of coal seams and the vertical extent of remnant pillars. Stress intensifies in pillars within stacked coal seams. In contrast, when pillars are undermined, stress is not transferred to depth below the mining panel.

Seismicity follows the trend of the negative *DMF* (Figures 8b–8d) which is related to the morphology of the mined panels. The section with the most negative *DMF* along the B-B′ transect corresponds to the area of the deepest mined coal seam Sonnenschein (Supplement 1 in Supporting Information S1) which was the earliest to be flooded (Figures S.2, and S.3 in Supporting Information S1).

8. Discussion

In the following subsections, we explore temporal and spatial evolution of flooding-induced seismicity in relation to mine water management. We discuss the parameters influencing the results of our stress calculations from Section 7 and assess their impact on seismicity. We compare our findings with patterns reported from other mines to support the role of stress arching.

8.1. Spatio-Temporal Evolution of Mine Water Levels and Induced Earthquakes

Rische et al. (2023) have suggested that flooding-induced seismicity occurs near underground galleries based on single-event localization. We use extended observation periods and improved event relocalization. Our results confirm the overall pattern of Rische et al. (2023) but also reveal spatial clustering of the events ∼300 m below galleries, concentrated within remnant pillars (Figure 3). The temporal distribution of seismicity is heterogeneous across the remnant pillars and reflects the flooding history. Variations in the depth of hydraulic connections to neighboring collieries, combined with differences in gallery depths, results in a non-uniform rise in water level

21699356, 2025, 9, Downloaded from https://agupubs.onlinelibrary.wiley.com/doi/10.1029/2025JB031323 by Karlsruher Institut für Technologie, Wiley Online Library on [17/09/2025]. See the Terms and Conditions (https://onlinelibrary.wiley.com/terms-and-conditions) on Wiley Online Library for rules of use; OA articles are governed by the applicable Creative Commons License

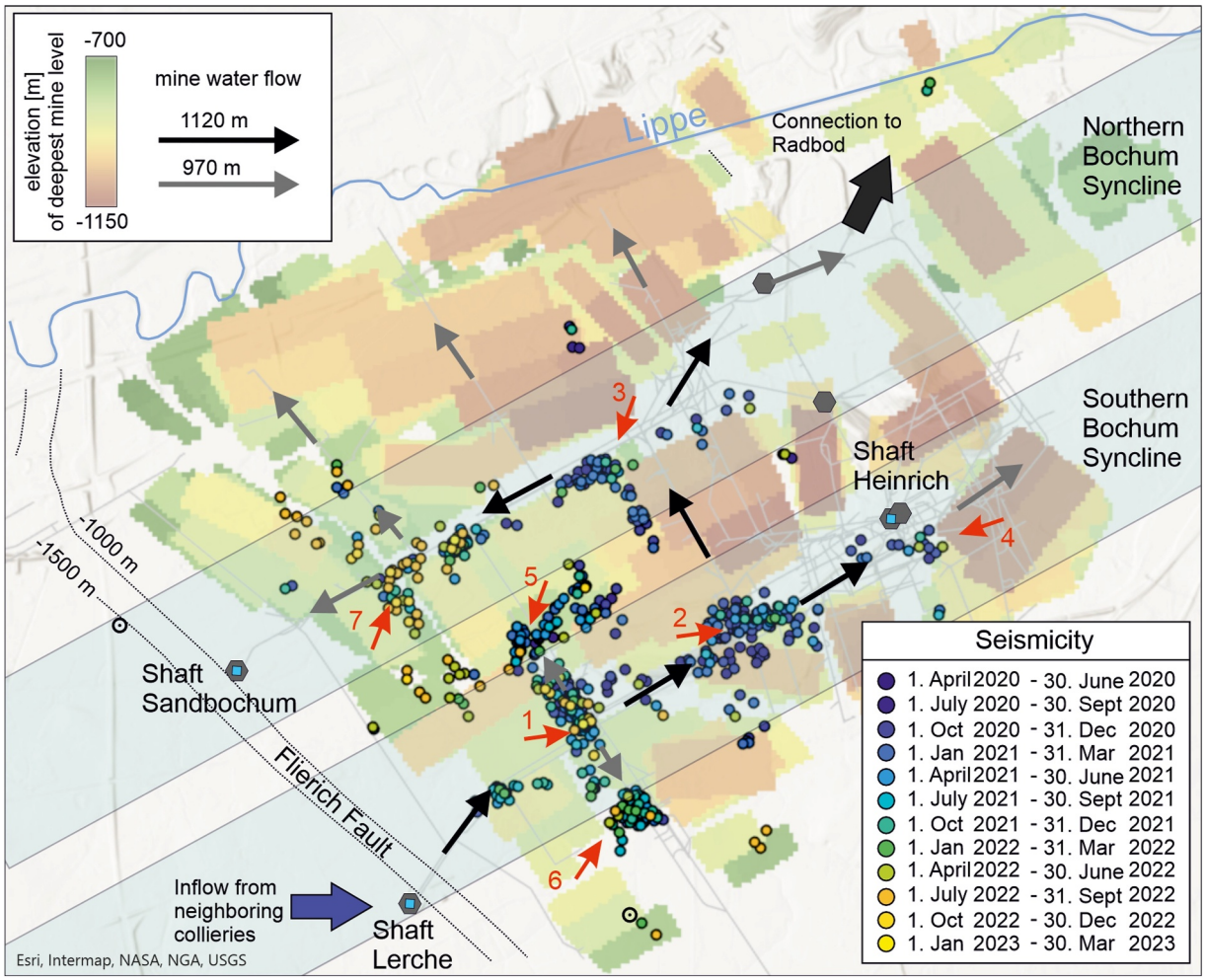

Figure 9. Relocated seismic events colored by date of occurrence. Mined panels are shaded according to the depth of the lowest mining level at each location. Black and gray arrows indicate interpreted water flow directions through galleries at −1,120 (black) and −970 m (gray) levels. Red arrows highlight seven specific positions discussed in the text.

(Figure S.8 in Supporting Information S1). Shaft Lerche enables inflow from the deeper western collieries into Heinrich-Robert mine (DMT, 2023), while connections to Radbod and Sandbochum transfer water to shallower northern mines. To capture this, we develop a simplified flow model based on the depths of the main galleries (−1,120 and −970 m) and hydraulic connections and compare it with seismic patterns in Figure 9.

During the early flooding (October 2019 to April 2020), water level in Heinrich Robert rose linearly, coinciding with a linear increase in seismicity at position 1. Once the water reached the −970 m level, hydraulic connections to neighboring collieries in particular mine Radbod became active, initiating parallel flooding and stabilizing the water level in Heinrich-Robert between May and July 2020. Seismicity also plateaued, still clustered at position 1. This position is located at the intersection of a shaft that connects galleries of multiple mine levels, including the −1,120 m gallery connecting Heinrich-Robert and shaft Lerche. The seismicity in position 1 is within a remnant pillar beneath shallow panels (−930 to −950 m), where zones of stress concentrations are also shallow. As the gallery in −1,120 m aligns with the extent of the EDZ of the mined panels, increased permeability in combination with short migration pathways enables rapid transmission of pore pressure changes to the depth of critically stressed fractures. This results in a fast seismic response, reflected in the simultaneous linear rise of water level and seismicity.

In August 2020, Radbod reached hydraulic equilibrium with Heinrich-Robert, and water levels resumed to a linear rise, though at a slower rate (Section 3, Figure S.8 in Supporting Information S1). Between August 2020

21699356, 2025, 9, Downloaded from https://agupubs.onlinelibrary.wiley.com/doi/10.1029/2025JB031323 by Karlsruher Institut für Technologie, Wiley Online Library on [17/09/2025]. See the Terms and Conditions (https://onlinelibrary.wiley.com/terms-and-conditions) on Wiley Online Library for rules of use; OA articles are governed by the applicable Creative Commons License

and August 2021, seismicity peaked for the entire observation period. The first and most prominent cluster formed at position 2 (Figure 9), followed by clusters at positions 3 and 4, associated with flooding of the deepest mining levels in Heinrich-Robert. By early 2021, clusters 5 and 6 emerged, coinciding with flooding of shallower sections in the southern Bochum Syncline. As flooding progressed, deeper seismicity declined by mid-2021, while shallower clusters became dominant, though with fewer events. While previous clusters were spatially associated with remnant pillars spanning the full vertical extent of the mine, cluster 5 was associated with a pillar truncated by a shallow mining level, not visible in Figure 9. This indicates that even partially severed pillars can still accumulate sufficient stress for reactivation, provided truncation occurs at the top, not the base. The final significant phase of induced seismicity occurred in mid-2022 in the northwestern part of the mine near shaft Sandbochum (position 7). Position 7 within the Northern Bochum Syncline corresponds to the shallowest part of the mine. A few additional seismic events were also recorded in the Southern Bochum Syncline.

Overall, the temporal occurrence of seismic clusters and their spatial distribution correlates with the depth of the deepest mining levels, which are controlled by the subsurface morphology of northeast-plunging synclines. Deeper areas show earlier seismicity, while shallower regions exhibit delayed responses due to pore pressure diffusion through the rock. Exceptions occur where galleries intersect stress concentration zones. In these areas, seismicity correlates directly with the linear rise in water level, due to enhanced hydraulic connectivity with neighboring collieries. This allows rapid pore pressure transmission. In contrast, areas without such galleries show delayed seismic responses, governed by pore pressure diffusion.

8.2. Numerical Model and Geomechanical Assessment of Flooding-Induced Events

To assess the location of seismicity during flooding, we apply two approaches. The static model represents a worst-case scenario and defines the maximum affected volume for a given water level. Unlike the transient model, it neglects pore pressure diffusion, which is governed by permeability (Kivi et al., 2024). This leads to larger changes in pore pressure in the static model compared to those in the transient model for the same recorded mine water levels (Figure S.14 in Supporting Information S1). While the static model cannot explain the frequency of events, it is beneficial for estimating the lateral and vertical zoning, where *DMF* is negative. It requires fewer computational resources and less information on subsurface flow behavior, which is often poorly constrained. We integrate both modeling approaches and examine how mine geometry influences stress redistribution and dominates the background stress field (Section 8.2.1). We further compare the temporal evolution of volumes with negative *DMF* for the different modeling approaches (Section 8.2.2) and relate these changes to the observed sequence of induced seismic events. Finally, we assess the potential for larger fault reactivation (Section 8.2.3) and discuss its implications for seismic hazard in the context of mine flooding.

8.2.1. Stress Redistribution in Different Tectonic Regimes

For model B we consider two ambient stress regimes that have been reported: a normal faulting regime (Niederhuber et al., 2025), and a strike-slip regime (Kruszewski et al., 2021; Müller, 1991). In both scenarios, the zero-shear-stress boundary condition at the mine walls leads to stress redistribution around the mined panels, resulting in stress arching (Brady & Brown, 2004). Independent of the regional tectonic regime, the local stress redistribution shows similar patterns (Figure S.16b in Supporting Information S1, positions 1 and 2). Directly above and below the mined panels, the unloading (shown in Figure S.12 in Supporting Information S1 for the regional normal faulting regime, but also valid for the regional strike slip regime because $S_{H\max} > S_V = S3$) results in a local thrust faulting stress regime. This aligns with the mining-induced microseismicity that has been described by Wehling-Benatelli (2010). At the pillar boundaries, horizontal stresses are zero as the mined panels cannot transfer horizontal stresses. Here, increased vertical stress due to stress arching combined with the absence of horizontal stress leads to spalling as the dominant failure mechanism (Figure S.12 in Supporting Information S1). Within the pillars, our results indicate a local normal faulting regime ($S_{zz} = S_V > S_{yy} > S_{xx}$), consistent with seismicity observed on steeply dipping normal faults (Bischoff et al., 2010; Wehling-Benatelli, 2010).

We cannot determine the full impact of mining-induced pillar bursts and fault reactivation beneath the mine on deeper sections. However, following initial rock failure (e.g., from mining or blasting), failure progresses within pillars and along panel edges until stress equilibrium is reached (Iannacchione et al., 2005). It is likely that rock failure propagates and causes weakening at greater depths. The extent and nature of failure depend on the local stress state and the mechanical properties of the surrounding rock. Tensile failure typically remains confined to

21699356, 2025, 9, Downloaded from https://agupubs.onlinelibrary.wiley.com/doi/10.1029/2025JB031323 by Karlsruher Institut für Technologie, Wiley Online Library on [17/09/2025]. See the Terms and Conditions (https://onlinelibrary.wiley.com/terms-and-conditions) on Wiley Online Library for rules of use; OA articles are governed by the applicable Creative Commons License

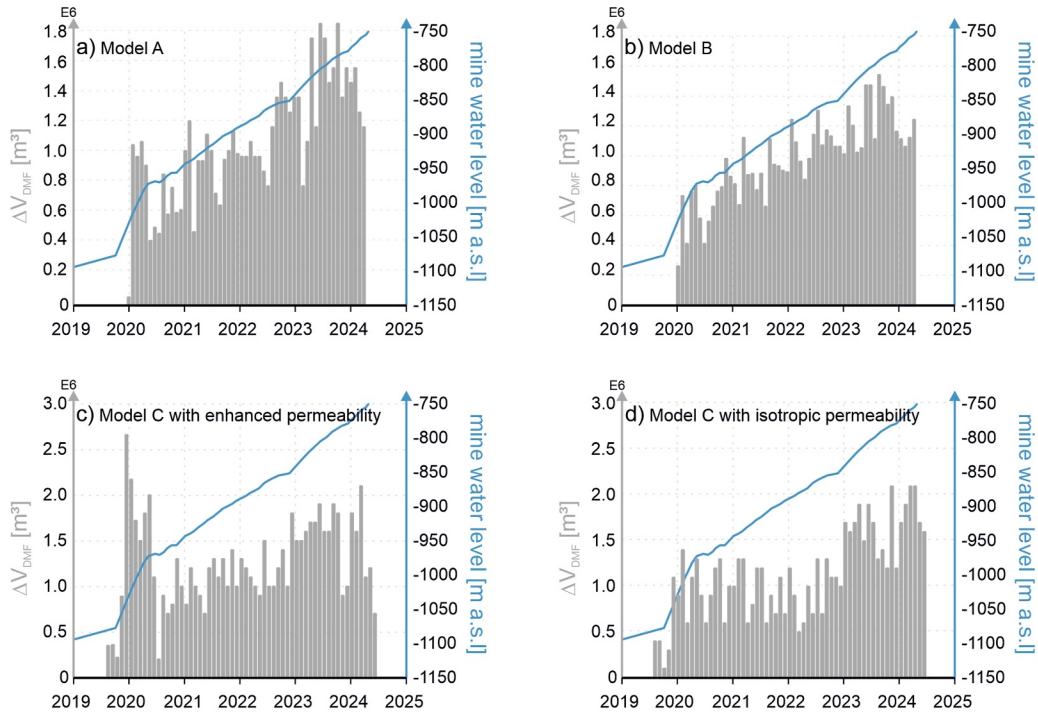

Figure 10. Temporal evolution of ΔV_{DMF} compared to water level. (a–c) results of model A–C (with locally enhanced permeability) and (d) results of model C (with homogeneous permeability throughout the model).

areas near the mined panels, whereas shear failure can extend farther from the excavation (Yin et al., 2016). Both failure modes disrupt the rock structure and significantly increase permeability, as demonstrated by S. Wang et al. (2013).

Observations of the non-uniform spatial distribution of methane degassing at the surface above the Heinrich-Robert mine (Thielmann, 2000) support the assumption of zones of enhanced permeability within the mine. Methane emissions concentrate above pillar zones and do not correlate with fault zones or mined panels (Supplement 10 in Supporting Information S1). This pattern aligns with areas of critical stress concentration derived in model D and supports the hypothesis, that localized shear failure within the remnant pillars leads to stress-dependent increases in permeability. The observation of methane degassing, several hundred meters above the mining panels indicates that zones of critical stress concentration extend vertically over considerable distances, as proposed by the numerical models. Furthermore, material behavior transitions from elastic to more plastic (Jiang et al., 2016); Park and Ash (1985); Revuzhenko, 1978). This reduces stress magnitudes and makes subsequent seismicity during flooding less likely.

During flooding, the additional water load on the panels increases the total vertical stress. Since pore pressure rises by the same amount, effective vertical stress should remain unchanged. However, our simulation reveals changes in the minimum principal stress component (Figure 7c). These changes can be attributed either to (a) an inclined stress tensor, where horizontal stress components contribute to $S3$, or (b) an imbalance between pore pressure and water load. The latter acts instantaneously on the mining panels, whereas pore pressure changes are delayed at greater depths, depending on permeability. Such time lags have also been observed during reservoir impoundment, where delays between filling and induced seismicity have been reported (Roeloffs, 1988). Geometric and poroelastic effects further influence stress redistribution within the pillars, resulting in a greater reduction in the vertical than in the horizontal direction (Figures 7a and 7b).

8.2.2. Temporal Distribution of Volumes With Negative DMF

Models A and B, which feature planar mining panels, show an almost linear increase in negative *DMF* volume ΔV_{DMF} over time (Figures 10a and 10b). Model A shows higher absolute ΔV_{DMF} compared to model B. This difference results from the depth distribution of the mining panels: in model A, all panels are located at −1,000 m,

21699356, 2025, 9, Downloaded from https://agupubs.onlinelibrary.wiley.com/doi/10.1029/2025JB031323 by Karlsruher Institut für Technologie, Wiley Online Library on [17/09/2025]. See the Terms and Conditions (https://onlinelibrary.wiley.com/terms-and-conditions) on Wiley Online Library for rules of use; OA articles are governed by the applicable Creative Commons License

whereas model B includes one panel at a shallower depth of −750 m, close to the final water level in the simulation (Figure 4). Due to the elevated panel, associated stress concentrations are also at shallower depths and faults therein are reactivated later, particularly when the flooding level exceeds the panel depth. This reduces the ΔV_{DMF} during the early stages of the simulation compared to model A, where all panels are situated at the same depth.

In model C, we investigate the influence of enhanced permeability based on the *DMF* criterion introduced in Section 6.2. We compare a model with homogeneous permeability (Figure 10d) to one with stress-dependent, locally enhanced permeability (Figure 10c). Under homogeneous conditions, ΔV_{DMF} remains lower and does not exhibit a peak during the period of highest mine water level rise (Figure 10d). Instead, a delayed increase in ΔV_{DMF} occurs approximately 3 years later. The enhanced permeability model shows a pronounced increase ΔV_{DMF} during the rapid rise in mine water level between late 2019 and early 2020 (Figure 10c). In the later flooding phase, ΔV_{DMF} stabilizes over time, with minor fluctuations.

Although the overall temporal trend of ΔV_{DMF} generally reflects the measured seismicity, a significant time shift is evident. The highest seismicity occurred between mid-2020 and mid-2021, approximately one year later than predicted by the model C. This delay is likely attributed to the following effects:

1. Simplified mine geometry with mining in a single coal seam: In the model the panels follow a generalized subsurface morphology adapted to the Bochum Synclines, with an average depth between −1,000 and −1,100 m. This depth reflects the average depth of the lowest coal seam Sonnenschein in the Heinrich-Robert mine (Figure S.2 in Supporting Information S1). Although the deepest mining levels are flooded first, seismicity does not necessarily concentrate at these depths (Figure 9). For flooding-induced seismicity, stress concentrations require the presence of pillars laterally constrained by at least two mined-out panels at similar depths. In the southern and western parts of the mine, deeper panels exist below −1,000 m but do not form pillars (Figure 9). To address this, we recalculated model C for panels located at higher levels (−900 to −1,000 m). This results in a delayed onset of ΔV_{DMF} (Figure S.18b in Supporting Information S1 compared to Figure S.18c in Supporting Information S1) and aligns more closely with seismicity at Heinrich-Robert mine from 2019 to 2022 (Figure S.18a in Supporting Information S1).
2. Representation of mined panels as open voids: In the model, mined panels are implemented as open voids, where fluid velocities are significantly higher than in porous media, and pore pressure acts immediately on void boundaries. However, in the Heinrich-Robert mine some panels have been actively backfilled, while most remain unfilled with a high probability for massive roof collapse. Initially, the goaf is air-filled, and water must displace this air to saturate the voids. This displacement is governed by capillary forces, which are more pronounced in smaller pores, reducing hydraulic conductivity and introducing a time lag. Air compressibility further resists fluid flow, slowing pore pressure equilibration. Unsaturated zones contribute minimally to flow, effectively lowering permeability. Once saturation is reached, pressure propagates more rapidly through the incompressible water column. Additionally, void space is reduced due to compaction, and flow is influenced by dams constructed within galleries. Despite reduced lateral conductivity, vertical permeability often increases due to fracturing of the surrounding rock (see Section 8.2.1). Overall, the sequences of events and ΔV_{DMF} reflects a superposition of effects that reduce horizontal and increase vertical permeability.
3. Fault orientation and reactivation potential: We investigate negative *DMF* values considering the most critical fault orientations (Supplement 7 in Supporting Information S1). Most fractures are expected to trend NW-SE, parallel to the larger normal faults consistent with dipmeter log data indicating NNW to NW orientations in the study area (Allgaier et al., 2023). However, the fault sets have formed during orogeny and subsequent uplift under a uniform far-field stress state. Within the mining area, the local stress field differs in both magnitude and orientation. Fracture sets that are not optimally oriented for reactivation require higher pore pressure for reactivation. This, along with local variations in the coefficient of friction contributes to the observed time shift between model predictions and seismicity. Alber and Schwarz (2015) have demonstrated that the friction coefficient varies widely depending on coal content.

8.2.3. Consequences for Larger Fault Reactivation

Within the Eastern Ruhr Area several major normal faults, strike-slip faults, and thrust faults are known (Allgaier et al., 2024). If reactivated they would have the potential of creating earthquakes of a large magnitude. However, they have not been active prior to, during, or after mining and flooding activities (Grünthal & Bosse, 1996; Rische

21699356, 2025, 9, Downloaded from https://agupubs.onlinelibrary.wiley.com/doi/10.1029/2025JB031323 by Karlsruher Institut für Technologie, Wiley Online Library on [17/09/2025]. See the Terms and Conditions (https://onlinelibrary.wiley.com/terms-and-conditions) on Wiley Online Library for rules of use; OA articles are governed by the applicable Creative Commons License

et al., 2023), thus they might be not critically stressed in the contemporary stress field. This aligns with the results of Allgaier et al. (2024), who calculated slip tendencies for the Haus Aden water province using both deterministic and probabilistic approaches under normal faulting conditions, as also proposed by Niederhuber et al. (2025). Their analysis indicates a low probability of fault reactivation solely from increased pore pressure. To activate them the stresses need to be modified significantly.

Within the study area the most important faults are the Flierich and the Radbod faults which bound the Hammer Horst. The static model D shows that stress changes exceeding the *DMF* criterion and associated seismicity during flooding are primarily concentrated in the central part of the mine (Figure 8b), linked to stress arching, and not near the Flierich fault (Figures 8b and 8d). Therefore, our findings suggest that larger fault reactivation is unlikely. It remains uncertain whether minor faults encountered during mining at the mining level (Allgaier et al., 2024) extend to deeper levels. Stress concentrations confined beneath the pillar areas could reactivate these smaller faults resulting in low magnitude events. This is confirmed by the maximum recorded flooding-induced seismic event in "Verbundbergwerk Ost" with a magnitude of $M_L = 2.6$ (Rische et al., 2023).

Our analysis indicates that fault reactivation is confined to a narrow depth range, governed by stress concentrations, and is laterally restricted by the width of the pillar. Consequently, only sections of faults that extend beneath the pillar zones are susceptible to reactivation during flooding. Since earthquake magnitude correlates with the size of the reactivated fault plane, the resulting seismic events are inherently limited in magnitude (Wells & Coppersmith, 1994). The longest continuous pillar section, measuring 2.8 km, is located in the Northern Bochum syncline. However, due to widening of the pillar toward the northeast, the section exhibiting negative *DMF* is reduced to 2.3 km (Figure 8a). Within this zone, faults optimally oriented for reactivation are typically steeply dipping and oriented perpendicular to the pillar (Supplement 12 in Supporting Information S1). Focal mechanisms also indicate failure along steeply dipping faults, consistent with the fault and fracture orientations described by Allgaier et al. (2023).

Using the empirical relationships established by Wells and Coppersmith (1994), we estimate a maximum earthquake magnitude of Mag = 2.5, based on the rupture area. This is slightly less than the observed maximum earthquake magnitude (Mag = 2.6). This estimate assumes normal faulting, a vertical extent of 200 m for zones of negative *DMF* and an average pillar width of 200 m. In comparison, Alber (2023) has concluded a maximum magnitude of $M_L = 2.3$. However, the approach of Wells and Coppersmith (1994), which relates earthquake magnitude to rupture length or area, is based on larger-magnitude and deeper tectonic events and may not be fully applicable to smaller induced earthquakes. Abercrombie (2021) has highlighted ongoing debates regarding the interpretation of earthquake source parameters. Thus, there is some uncertainty in our estimate of the maximum magnitude. Our magnitude–frequency distribution (Figure S.9 in Supporting Information S1) shows a deficit in larger events, consistent with observations from other studies on induced seismicity (e.g., Bischoff et al., 2010). Verdon et al. (2017) have reported bimodal magnitude distributions and attributed deviations from the Gutenberg-Richter relationship to characteristic length scales that constrain rupture dimensions and event magnitudes. This supports our interpretation that only fault segments within critically stressed volumes around the mine are susceptible to reactivation. The limited extent of these volumes explains the observed deficit in larger-magnitude events. Shapiro et al. (2011) have found similar deficits during injection at the Soultz-sous-Forêts geothermal site and interpreted that only fault sections within the pressurized volume can be reactivated. In contrast to single-borehole stimulation, our mining-related approach accounts for both pore pressure distribution and stress concentrations arising from complex mine geometries.

8.3. Transfer of Concept to Flooding Induced Seismicity in Other Mines

Several high-resolution monitoring studies have been conducted in European coal districts to better understand flooding-induced seismicity. Alber (2017) has noted that flooding-induced seismicity in the Saar mining district exhibits lower magnitudes compared to seismicity during active mining, with hypocenters located below the former mining levels. Similar trends have been reported by Knoll (2016), Hassani et al. (2018), and Schütz and Konietzky (2016), for Schlema-Alberoda, where mining-induced events reached magnitudes up to $M_L = 2.9$, while flooding-induced events were typically below $M_L = 0$, with a maximum of $M_L = 1.8$ (Schütz & Konietzky, 2016). These events also occurred beneath the mined seams. At the Provence Colliery in the Gardanne Basin, Senfaute et al. (1997) have observed mining-induced events up to $M_L = 2.9$, whereas flooding-induced events at depths of 100–500 m below the mine level reached $M_L = 1.9$ (Dominique et al., 2022). Our study at

21699356, 2025, 9, Downloaded from https://agupubs.onlinelibrary.wiley.com/doi/10.1029/2025JB031323 by Karlsruher Institut für Technologie, Wiley Online Library on [17/09/2025]. See the Terms and Conditions (https://onlinelibrary.wiley.com/terms-and-conditions) on Wiley Online Library for rules of use; OA articles are governed by the applicable Creative Commons License

the Heinrich-Robert mine confirms this trend: flooding-induced events are of lower magnitude and concentrate below the mining level. During active mining, the maximum recorded event was $M_L = 3.3$ (Bischoff et al., 2010), while during flooding it was $M_L = 2.6$ (Rische et al., 2023), with highest magnitudes occurring in the initial flooding phase (Figure S.8 in Supporting Information S1).

However, the mechanisms proposed to explain flooding-induced seismicity differ between earlier studies and our approach: Alber (2017) for the Saar district and Knoll (2016) for Schlema-Alberoda have concluded that increased pore pressure reduces the effective normal stress on pre-existing faults. Hassani et al. (2018) have attributed seismicity in Schlema-Alberoda to weakening of the fault strength by increased pore pressure. For the Gardanne mine, Dominique et al. (2022) have concluded that seismicity results from reduced effective stress and in Namjesnik et al. (2022) it is indicated that flooding leads to stress redistribution. Namjesnik et al. (2021) have attributed the spatial distribution of seismicity to both known faults identified during mining and assumed faults inferred from seismicity patterns below the mined levels in Gadanne. The assumed fault lengths correspond to the location and extent of the remnant pillars. However, these faults had not been described during mining in the adjacent mine panels, which should have intersected them.

In our approach, we also attribute flooding-induced seismicity to changes in pore pressure and thus effective stress. But to explain the spatial clustering of microseismicity beneath remnant pillars, we apply the concept of stress arching. This mechanism confines the affected volume and thereby limits the maximum possible magnitudes (see Section 8.2.4). As a result, seismic activity decreases over time, as observed at the Heinrich-Robert mine (Figure S.8 in Supporting Information S1). A similar temporal trend has been documented in the Saar mining district (Alber, 2017) and in Schlema-Alberoda (Konietzky, 2014). In the latter case, this supports a mechanism involving stress concentration controlled by mine design, in combination with rising pore pressure. This contradicts Hassani et al. (2018), who has attributed seismicity to fault weakening, and Knoll (2016), who has expected seismicity to occur at greater distances along permeable fault zones.

In Gardanne mine, seismicity is episodic and temporally correlated with rainfall reflecting the open hydrological system. However, the spatial pattern of events, especially Swarms 3 and 4 is associated with the location of remnant pillars (Figure 17a in Namjesnik et al., 2021), similar to the patterns observed in our study area. In difference, the Gardanne mine is located in a tectonically active region, where natural seismicity reaches magnitudes of Mw 5.7–6.1 (Baroux et al., 2003). Focal mechanisms and stress inversions indicate a regional transpressive to compressive stress regime (Baroux et al., 2001; Delacou et al., 2004), further supported by in situ stress measurements within the mine (Gaviglio et al., 1996). Focal mechanisms of flooding-induced events show a clear normal faulting (Dominique et al., 2022), contradicting the regional stress field and indicating that the ambient stress state is locally altered within the pillars to a normal faulting regime. This effect, linked to stress arching, is also evident in our numerical models (see Section 8.2.1). Thus, our approach explains both the spatial distribution of Swarm 3 and 4 in Gardanne and the normal faulting focal mechanisms. This highlights that reduced effective stress within zones of localized stress concentration due to arching is a dominant mechanism in Gardanne, consistent with our findings in the Heinrich-Robert mine.

8.4. Comparison to Natural Earthquake Swarms and Injection Induced Seismicity

Natural and induced earthquake swarms describe series of earthquakes that occur closely together in time and space and unlike aftershocks, are not related to a main event. This clustering is also observed in flooding-induced earthquakes (Alber, 2017; Hassani et al., 2018; Knoll, 2016; Namjesnik et al., 2022; see Section 8.1).

Hypocenters of natural and injection-induced swarms propagate away from the first events or from the injection point, respectively (Danre et al., 2024). Natural earthquake swarms occur under relatively stable tectonic or hydrodynamic conditions and seem to be controlled by pressure fluctuations under the prevailing stress field (Danre et al., 2024), though the underlying mechanisms remain a subject of ongoing investigation (Shelly, 2024).

Fluid-induced earthquakes close to injection wells are dominated by the volume of the injected fluids (e.g., McGarr, 2014). The propagation of the seismicity front can be described by diffusion approaches using statistical distributions of fault criticality, resulting in a square root relationship for the spatial occurrence of seismicity with time (Shapiro et al., 1997). Other studies have suggested that deformation in the initial fluid injection phase can also be aseismic (Guglielmi et al., 2015) and that aseismic slip can transfer and redistribute stresses and trigger delayed seismicity (Eyre et al., 2019; Wang & Dunham, 2022; Wei et al., 2015; Wynants-Morel et al., 2020). In

21699356, 2025, 9, Downloaded from https://agupubs.onlinelibrary.wiley.com/doi/10.1029/2025JB031323 by Karlsruher Institut für Technologie, Wiley Online Library on [17/09/2025]. See the Terms and Conditions (https://onlinelibrary.wiley.com/terms-and-conditions) on Wiley Online Library for rules of use; OA articles are governed by the applicable Creative Commons License

this framework, distributed asperities, initial stress conditions, and fault criticalities determine the scaling of earthquake magnitudes with injected fluid volume (Danre et al., 2024). De Barros et al. (2021) have shown that while fluid pressure diffuses nearly radially, aseismic slip occurs on an elongated ellipse, with the major axis aligned with the major principal stress orientation.

In our study, we observe temporal migration of seismic clusters that cannot be explained solely by diffusive processes. Within the mine, heterogeneously distributed air-filled voids and strong permeability contrasts defined by the damage zones around panels, shafts, and galleries enable rapid, non-diffusive fluid migration. Consequently, pore pressure and seismicity do not increase continuously and are not directly correlated with the volume of flooding water. Instead, pressure evolution depends on the size of the water province, the volume of mined panels, and the hydraulic connectivity between them via shafts and galleries. In particular, the cluster at position 1 (Figure 9) can be explained by non-diffusive processes, where critically stressed volumes are hydraulically connected through galleries.

9. Conclusions and Outlook

We present a precise localization of seismicity during flooding in the Heinrich-Robert mine. By integrating these observations with modeled stress distributions, we show that the temporal occurrence and spatial pattern of seismic events are primarily driven by a combination of stress heterogeneities resulting from anthropogenic activities and pressure changes. Seismicity is localized within confined volumes defined by the geometry of the mine and its hydraulic structure. In this context, classical diffusion models are of limited applicability, as they cannot fully account for the spatial and temporal variability of effective injection points and the resulting complex stress and pressure distribution.

These findings have broader relevance beyond mining contexts. Similar mechanisms may govern fluid-induced seismicity in highly conductive fault zones and karstic systems, where hydraulic connectivity controls stress transfer. The concept of localized stress concentration due to arching, combined with pore pressure changes, offers a robust framework for understanding the distribution and magnitude of fluid-related natural earthquake swarms in tectonically complex regions.

In conclusion, we attribute this flooding-induced seismicity to localized stress arching in the pillar zones and changes in pore pressure. While the effective vertical stress remains nearly unchanged, rising pore pressure reduces the effective horizontal stress, thereby increasing the likelihood of shear failure independently of the regional tectonic regime. Focal mechanisms, as previously reported, have indicated reactivation of steeply dipping normal faults subparallel to the maximum horizontal stress and spatially limited.

The geometry and especially the width of the pillars are crucial parameters controlling both spatial extent and magnitude of increased stress and thereby govern permeability enhancement. The affected volume may extend vertically to the surface supported by observations of methane degassing above the pillars. We conclude that the presence of these volumes together with the mine water management and the depth distribution of the lowest mining level govern the temporal occurrence of induced seismicity. Therefore, seismicity cannot be solely attributed to fluctuations in mine water level.

Future flooding of the Heinrich Robert mine may reactivate faults located slightly below and, more prominently, above the uppermost mining level. For reliable seismic hazard assessment during future flooding, the overlying Cretaceous and Quaternary strata, particularly the Emscher Marls, must be considered due to their distinct rheological and hydraulic properties.

In summary, flooding-induced seismicity in mines is not primarily controlled by far-field tectonic stresses or the volume of inflowing water. Instead, the location, timing, and extent of fault reactivation is governed by pore pressure increase in combination with localized stress concentrations below the lowest mining level. These conditions arise from the complex geometry of the mine and its hydraulic connectivity.

These findings offer the potential to reduce the risk of stronger seismic events during mining and flooding through selection of appropriate mine design prior to excavation. The integration of numerical modeling and event relocation data has shown that most seismic events do not occur on nearby larger natural faults, which accounts for the observed frequency-magnitude distribution and the deficit of larger events. Consequently, future seismicity is also likely to remain limited in magnitude, a critical consideration for this densely populated region.

21699356, 2025, 9, Downloaded from https://agupubs.onlinelibrary.wiley.com/doi/10.1029/2025JB031323 by Karlsruher Institut für Technologie, Wiley Online Library on [17/09/2025]. See the Terms and Conditions (https://onlinelibrary.wiley.com/terms-and-conditions) on Wiley Online Library for rules of use; OA articles are governed by the applicable Creative Commons License

Conflict of Interest

The authors declare no conflicts of interest relevant to this study.

Data Availability Statement

The seismological data are included in the International Federation of Digital Seismograph Networks (FDSN) and are stored within the BGR. They can be accessed by Friederich et al. (2020). Mine Geometry and location as well as time series of mine water levels are accessed from RAG-BID (2023). This is a service that provides information from RAG on current topics as well as on former mining activities in North Rhine-Westphalia and the Saarland. Initially, the data protection notice must be accepted. The mining areas can be viewed under "Mining Activities > Mining since 1,969." The data on mine water levels can be accessed via "Water Management > Mine Water Levels." The drilling report of Pelkum-2 is available upon request from the Geological Survey of North Rhine-Westphalia (GD-NRW, 2025).

Acknowledgments
This work was carried out in scientific cooperation with GD NRW as part of the FloodRisk project (Grant FKZ:03G0893 A-E) funded by GEO:N a funding program sponsored by the German Federal Ministry of Education and Research. We thank all project partners for their invaluable expert advice and contributions. We thank the technicians Bernhard Klotz and Lothar Kühne for setting up and maintaining the seismological network. A special thanks to RAG for their support in releasing and providing the necessary data for our research. We thank the editor R. Abercrombie, the associate editor, and the two reviewers for their helpful and constructive comments and suggestions, which significantly improved the manuscript. Open Access funding enabled and organized by Projekt DEAL.

References

Abdi, H., Nguyen, T. S., Evgin, E., Fall, M., & Su, G. (2010). Coupled hydro-mechanical analysis of excavation damage zones around an underground opening in sedimentary rock. In *Proceedings of the COMSOL conference 2010 Boston*.

Abercrombie, R. E. (2021). Resolution and uncertainties in estimates of earthquake stress drop and energy release. *Philosophical Transactions of the Royal Society A*, *379*(2196), 20200131. https://doi.org/10.1098/rsta.2020.0131

ahu AG. (2017). Gutachten zur Prüfung möglicher Umweltauswirkungen des Einsatzes von Abfall-und Reststoffen zur Bruch-Hohlraumverfüllung in Steinkohlenbergwerken in Nordrhein-Westfalen, TEIL 1—Detailbericht 1: Hydrogeologische Systembeschreibung und Auffälligkeiten an der Tagesoberfläche: Im Auftrag von: Ministerium für Klimaschutz, Umwelt, Landwirtschaft, Natur-und Verbraucherschutz des Landes Nordrhein-Westfalen and Ministerium für Wirtschaft, Energie, Industrie, Mittelstand und Handwerk des Landes Nordrhein-Westfalen. Report. Retrieved from http://www.umweltauswirkungen-utv.de/gutachten_2/final/Detailbericht_1.pdf

Alber, M. (2017). Gutachten zur Erschütterungsentwicklung während des Grubenwasseranstiegs auf -320 mNN in den Wasserprovinzen Reden und Duhamel. Report. *Alber Geomechanik*. https://geodaten.rag.de/bid/tree/GenV/Saar/Wass_V/He_u_Ei_Grubw_DH/7_Alber_Ersch%C3%BCtterungen/Gutachten%20zur%20flutungsbedingten%20Ersch%C3%BCtterungenentwicklung%20Saar%20%2004_04_2017.pdf

Alber, M. (2023). Gutachten zur Erschütterungsentwicklung während des Grubenwasseranstiegs auf -380 mNHN im Wasserhebungsbereich Haus Aden: Auftraggeber: RAG Aktiengesellschaft.

Alber, M., & Fritschen, R. (2011). Rock mechanical analysis of a Ml= 4.0 seismic event induced by mining in the Saar district, Germany. *Geophysical Journal International*, *186*(1), 359–372. https://doi.org/10.1111/j.1365-246X.2011.05047.x

Alber, M., Fritschen, R., Bischoff, M., & Meier, T. (2009). Rock mechanical investigations of seismic events in a deep longwall coal mine. *International Journal of Rock Mechanics and Mining Sciences*, *46*(2), 408–420. https://doi.org/10.1016/j.ijrmms.2008.07.014

Alber, M., & Schwarz, J. (2015). Experiments on low-friction discontinuities from carboniferous strata in the Ruhr Mining District. In *ISRM EUROCK. Symposium conducted at the meeting of ISRM*.

Allgaier, F., Busch, B., Niederhuber, T., Quandt, D., Müller, B., & Hilgers, C. (2023). Fracture network characterisation of the naturally fractured upper Carboniferous sandstones combining outcrop and wellbore data, Ruhr Basin, Germany. *Zeitschrift der Deutschen Gesellschaft für Geowissenschaften*, *173*(4), 599–623. https://doi.org/10.1127/zdgg/2023/0369

Allgaier, F., Niederhuber, T., Busch, B., Müller, B., & Hilgers, C. (2024). Post-mining related reactivation potential of faults hosted in tight reservoir rocks around flooded Coal Mines, eastern Ruhr Basin, Germany. *Geomechanics for Energy and the Environment*, *38*, 100560. https://doi.org/10.1016/j.gete.2024.100560

Arabasz, W. J., Nava, S. J., McCarter, M. K., Pankow, K. L., Pechmann, J. C., Ake, J., & McGarr, A. (2005). Coal-mining seismicity and ground-shaking hazard: A case study in the trail Mountain area, emery County, Utah. *Bulletin of the Seismological Society of America*, *95*(1), 18–30. https://doi.org/10.1785/0120040045

Azizmohammadi, S., & Matthäi, S. K. (2017). Is the permeability of naturally fractured rocks scale dependent? *Water Resources Research*, *53*(9), 8041–8063. https://doi.org/10.1002/2016WR019764

Baroux, E., Bethoux, N., & Bellier, O. (2001). Analyses of the stress field in southeastern France from earthquake focal mechanisms. *Geophysical Journal International*, *145*(2), 336–348. https://doi.org/10.1046/j.1365-246x.2001.01362.x

Baroux, E., Pino, N. A., Valensise, G., Scotti, O., & Cushing, M. E. (2003). Source parameters of the 11 June 1909, Lambesc (Provence, southeastern France) earthquake: A reappraisal based on macroseismic, seismological, and geodetic observations. *Journal of Geophysical Research*, *108*(B9). https://doi.org/10.1029/2002JB002348

Biot, M. A. (1941). General theory of three-dimensional consolidation. *Journal of Applied Physics*, *12*(2), 155–164. https://doi.org/10.1063/1.1712886

Bischoff, M., Cete, A., Fritschen, R., & Meier, T. (2010). Coal mining induced seismicity in the Ruhr area, Germany. *Pure and Applied Geophysics*, *167*(1–2), 63–75. https://doi.org/10.1007/s00024-009-0001-8

Bohnsack, D., Potten, M., Freitag, S., Einsiedl, F., & Zosseder, K. (2021). Stress sensitivity of porosity and permeability under varying hydrostatic stress conditions for different carbonate rock types of the geothermal Malm reservoir in southern Germany. *Geothermal Energy*, *9*(1), 15. https://doi.org/10.1186/s40517-021-00197-w

Brady, B. H. G., & Brown, E. T. (2004). *Rock mechanics for underground mining* (3ed.). Springer Science and Business Media. https://doi.org/10.1007/978-1-4020-2116-9

Brix, M. R., Drozdzewski, G. H., Greiling, R. O., Wolf, R., & Wrede, V. (1988). The N variscan margin of the Ruhr coal district (Western Germany): Structural style of a buried thrust front? *Geologische Rundschau*, *77*(1), 115–126. https://doi.org/10.1007/BF01848679

Byerlee, J. (1978). Friction of rocks. *Pure and Applied Geophysics*, *116*(4–5), 615–626. https://doi.org/10.1007/BF00876528

Chen, Y., Selvadurai, A. P. S., & Liang, W. (2019). Computational modelling of groundwater inflow during a longwall coal mining advance: A case study from the Shanxi province, China. *Rock Mechanics and Rock Engineering*, *52*(3), 917–934. https://doi.org/10.1007/s00603-018-1603-1

21699356, 2025, 9, Downloaded from https://agupubs.onlinelibrary.wiley.com/doi/10.1029/2025JB031323 by Karlsruher Institut für Technologie, Wiley Online Library on [17/09/2025]. See the Terms and Conditions (https://onlinelibrary.wiley.com/terms-and-conditions) on Wiley Online Library for rules of use; OA articles are governed by the applicable Creative Commons License

Chlebowski, D., & Burtan, Z. (2021). Mining-induced seismicity during development works in coalbeds in the context of forecasts of geomechanical conditions. *Energies*, *14*(20), 6675. https://doi.org/10.3390/en14206675

Comsol, M. (2021). *Slope stability in an embankment dam. Created in COMSOL multiphysics 5.6*. Comsol Multiphysics. Retrieved from https://www.comsol.com/model/slope-stability-in-an-embankment-dam-54461

Contrucci, I., Namjesnik, D., Niemz, P., Primo, P., Kotyrba, A., Mutke, G., et al. (2023). European feedback on post-mining seismicity. *Journal of Sustainable Mining*, *22*(3), 195. https://doi.org/10.46873/2300-3960.1385

Creutzburg, H. (1963). Zur Wärmeleitfähigkeit des paläozoischen Gebirges in der Bohrung Münsterland 1. In *Fortschritte in der Geologie von Rheinland und Westfalen: Die Aufschlussbohrung Münsterland 1.: Ein Symposium. 568 S., 131 Abb., 64 Tab., 48 Taf* (Vol. 11, pp. 395–402). Landesbetrieb.

Danré, P., Garagash, D., De Barros, L., Cappa, F., & Ampuero, J. P. (2024). Control of seismicity migration in earthquake swarms by injected fluid volume and aseismic crack propagation. *Journal of Geophysical Research: Solid Earth*, *129*(1), e2023JB027276. https://doi.org/10.1029/2023JB027276

De Barros, L., Wynants-Morel, N., Cappa, F., & Danré, P. (2021). Migration of fluid-induced seismicity reveals the seismogenic state of faults. *Journal of Geophysical Research: Solid Earth*, *126*(11), e2021JB022767. https://doi.org/10.1029/2021JB022767

Delacou, B., Sue, C., Champagnac, J. D., & Burkhard, M. (2004). Present-day geodynamics in the Bend of the Western and central Alps as constrained by earthquake analysis. *Geophysical Journal International*, *158*(2), 753–774. https://doi.org/10.1111/j.1365-246X.2004.02320.x

DMT. (2023). Grubenwasserentwicklung in der Wasserprovinz Haus Aden beim Wasseranstieg auf -380 mNHN: Auftraggeber: RAG Aktiengesellschaft.

Dominique, P., Aochi, H., & Morel, J. (2022). Triggered seismicity in a flooded former coal mining basin (Gardanne area, France). *Mine Water and the Environment*, *41*(2), 317–334. https://doi.org/10.1007/s10230-022-00860-z

Drobniewski, M., Balzer, I., Frankenhoff, H., & Witthaus, H. (2017). Mine water management in the Ruhr coalfield.

Drozdzewski, G. H. (1993). The Ruhr coal basin (Germany): Structural evolution of an autochthonous foreland basin. *International Journal of Coal Geology*, *23*(1–4), 231–250. https://doi.org/10.1016/0166-5162(93)90050-k

Drozdzewski, G. H., Hoth, P., Juch, D., Littke, R., Vieth, A., & Wrede, V. (2009). The Pre-Permian of NW-Germany structure and coalification map. *Zeitschrift der Deutschen Gesellschaft für Geowissenschaften*, *160*(2), 159–172. https://doi.org/10.1127/1860-1804/2009/0160-0159

Duda, M. (2011). *An integrated experimental study on elastic and inelastic properties of sandstones and the role of transient pore pressure*. [Doctoral thesis]. Ruhr-University Bochum.

Durucan, S., & Edwards, J. S. (1986). The effects of stress and fracturing on permeability of coal. *Mining Science and Technology*, *3*(3), 205–216. https://doi.org/10.1016/S0167-9031(86)90357-9

Esterhuizen, E., Mark, C., & Murphy, M. M. (2010). The ground response curve, pillar loading and pillar failure in coal mines. In *Proceedings of the 29th international conference on ground control in mining*.

Eurostat. (2024). Coal production and consumption statistics. *Statistics Explained*. Retrieved from https://ec.europa.eu/eurostat/statistics-explained/index.php?title=Coal_production_and_consumption_statistics

Eyre, T. S., Eaton, D. W., Garagash, D. I., Zecevic, M., Venieri, M., Weir, R., & Lawton, D. C. (2019). The role of aseismic slip in hydraulicfracturing—induced seismicity. *Science Advances*, *5*(8), eaav7172. https://doi.org/10.1126/sciadv.aav7172

Foulger, G. R., Wilson, M. P., Gluyas, J. G., Julian, B. R., & Davies, R. J. (2018). Global review of human-induced earthquakes. *Earth-Science Reviews*, *178*, 438–514. https://doi.org/10.1016/j.earscirev.2017.07.008

Fowkes, N., Hocking, G., Mason, D. P., Please, C. P., Kgatle, R., Yilmaz, H., & van der Merwe, N. (2015). Models for the effect of rising water in abandoned mines on seismic activity. *International Journal of Rock Mechanics and Mining Sciences*, *77*, 246–256. https://doi.org/10.1016/j.ijrmms.2015.04.011

Friederich, W., Fischer, K. D., Rische, M., & Hilgers, C., & Ruhr University Bochum. (2020). FloodRisk seismic network [Dataset]. *Federal Institute for Geosciences and Natural Resources (BGR, Germany)*. https://doi.org/10.7914/SN/YD_2020

Fritschen, R. (2010). Mining-Induced seismicity in the Saarland, Germany. *Pure and Applied Geophysics*, *167*(1–2), 77–89. https://doi.org/10.1007/s00024-009-0002-7

Gaviglio, P., Bigarre, P., Baroudi, H., Piguet, J.-P., & Monteau, R. (1996). Measurements of natural stresses in a Provence mine (Southern France). *Engineering Geology*, *44*(1–4), 77–92. https://doi.org/10.1016/S0013-7952(96)00041-5

Gibowicz, S. J. (2001). Seismicity induced by mining. In *Advances in geophysics. Advances in geophysics volume 44* (Vol. 32, pp. 1–74). Elsevier. https://doi.org/10.1016/S0065-2687(08)60426-4

Gibowicz, S. J. (2009). Seismicity induced by mining: Recent research. In *Advances in geophysics* (Vol. 51, pp. 1–53). Elsevier. https://doi.org/10.1016/S0065-2687(09)05106-1

Gibowicz, S. J., Harjes, H.-P., & Schäfer, M. (1990). Source parameters of seismic events at Heinrich Robert mine, Ruhr Basin. *Bulletin of the Seismological Society of America*, *80*, 88–109.

Gibowicz, S. J., & Lasocki, S. (2001). Seismicity induced by mining: Ten years later. In *Advances in geophysics. Advances in geophysics volume 44* (Vol. 44, pp. 39–181). Elsevier. https://doi.org/10.1016/S0065-2687(00)80007-2

Goldbach, O. D. (Ed.) (2009). *Seismic risks posed by mine flooding*.

Goldbach, O. D. (2010). *What is the seismic risk of mine flooding?* CSIR. Retrieved from https://researchspace.csir.co.za/dspace/handle/10204/4256

Greve, J., Busch, B., Quandt, D., Knaak, M., Hartkopf-Fröder, C., & Hilgers, C. (2023). Coupling heat conductivity and lithofacies of the coal-bearing upper Carboniferous in the eastern Ruhr Basin, NW Germany. *Zeitschrift der Deutschen Gesellschaft für Geowissenschaften*, *173*(4), 673–695. https://doi.org/10.1127/zdgg/2023/0350

Grünthal, G. (2014). Induced seismicity related to geothermal projects versus natural tectonic earthquakes and other types of induced seismic events in central Europe. *Geothermics*, *52*, 22–35. https://doi.org/10.1016/j.geothermics.2013.09.009

Grünthal, G., & Bosse, C. (1996). *Probabilistische Karte der Erdbebengefährdung der Bundesrepublik Deutschland-Erdbebenzonierungskarte für das Nationale Anwendungsdokument zum Eurocode 8: Scientific Technical Report STR96/10*. GeoForschungsZentrum Potsdam. https://doi.org/10.2312/GFZ.b103-96103

Guglielmi, Y., Cappa, F., Avouac, J. P., Henry, P., & Elsworth, D. (2015). Seismicity triggered by fluid injection–induced aseismic slip. *Science*, *348*(6240), 1224–1226. https://doi.org/10.1126/science.aab0476

Hahne, C., Schmidt, R., & Müller, W. (1982). Die Geologie des Niederrheinisch-Westfälischen Steinkohlengebirges: Einführung in das Steinkohlengebirge und seine Montangeologie. *Verl. Glückauf*.

Harnischmacher, S. (2010). Quantification of mining subsidence in the Ruhr District (Germany). Géomorphologie: Relief. *Processus, Environnement*, *16*(3), 261–274. https://doi.org/10.4000/geomorphologie.7965

21699356, 2025, 9, Downloaded from https://agupubs.onlinelibrary.wiley.com/doi/10.1029/2025JB031323 by Karlsruher Institut für Technologie, Wiley Online Library on [17/09/2025]. See the Terms and Conditions (https://onlinelibrary.wiley.com/terms-and-conditions) on Wiley Online Library for rules of use; OA articles are governed by the applicable Creative Commons License

Hassani, H., Hloušek, F., Alexandrakis, C., & Buske, S. (2018). Migration-based microseismic event location in the Schlema-Alberoda mining area. *International Journal of Rock Mechanics and Mining Sciences*, *110*, 161–167. https://doi.org/10.1016/j.ijrmms.2018.08.002

Helmholtz Centre Potsdam GFZ, German Research Centre for Geosciences, and GmbH, gempa. (2008). The SeisComP seismological software package [Computer Software]. *GFZ Data Services*. https://doi.org/10.5880/GFZ.2.4.2020.003

Hörl, M., & Rohde, C. (2024). Rigorous derivation of discrete fracture models for Darcy flow in the limit of vanishing aperture. *Networks and Heterogeneous Media*, *19*(1), 114–156. https://doi.org/10.3934/nhm.2024006

Huang, X., Ruan, H., Shi, C., & Kong, Y. (2021). Numerical simulation of stress arching effect in horizontally layered jointed rock mass. *Symmetry*, *13*(7), 1138. https://doi.org/10.3390/sym13071138

Hubbert, K., & Rubey, W. W. (1959). Role of fluid pressure in mechanics of overthrust faulting. *Geological Society of America Bulletin*, *70*(2), 115. https://doi.org/10.1130/0016-7606(1959)70[115:rofpim]2.0.co;2

Hund, K., La Porta, D., Fabregas, T. P., Laing, T., & Drexhage, J. (2020). *Minerals for climate action: The mineral intensity of the clean energy transition*. World Bank.

Iannacchione, A. T., Esterhuizen, G. S., Bajpayee, T. S., Swanson, P. L., & Chapman, M. C. (2005). Characteristics of mining-induced seismicity associated with roof falls and roof caving events. In *ARMA US rock mechanics/geomechanics symposium. Symposium conducted at the meeting of ARMA*.

IEA. (2024). Global critical minerals outlook 2024. IEA. Licence: CC BY 4.0. Retrieved from https://www.iea.org/reports/global-critical-minerals-outlook-2024

Jaeger, J. C., Cook, N. G. W., & Zimmerman, R. W. (2007). *Fundamentals of rock mechanics* (4). Blackwell Publ.

Jagert, F., Immenhauser, A., & Wohnlich, S. (2023). Hydrogeochemical modelling of groundwater in a fractured Carboniferous sandstone aquifer. *Grundwasser*, *28*(3), 225–242. https://doi.org/10.1007/s00767-023-00549-2

Jiang, L., Sainoki, A., Mitri, H. S., Ma, N., Liu, H., & Hao, Z. (2016). Influence of fracture-induced weakening on coal mine gateroad stability. *International Journal of Rock Mechanics and Mining Sciences*, *88*, 307–317. https://doi.org/10.1016/j.ijrmms.2016.04.017

Kelsall, P. C., Case, J. B., & Chabannes, C. R. (1984). Evaluation of excavation-induced changes in rock permeability. *International Journal of Rock Mechanics and Mining Sciences and Geomechanics Abstracts*, *21*(3), 123–135. https://doi.org/10.1016/0148-9062(84)91530-4

Kivi, I. R., Vilarrasa, V., Kim, K.-I., Yoo, H., & Min, K.-B. (2024). On the role of poroelastic stressing and pore pressure diffusion in discrete fracture and fault system in triggering post-injection seismicity in enhanced geothermal systems. *International Journal of Rock Mechanics and Mining Sciences*, *175*, 105673. https://doi.org/10.1016/j.ijrmms.2024.105673

Klose, C. D. (2007). Mine water discharge and flooding: A cause of severe earthquakes. *Mine Water and the Environment*, *26*(3), 172–180. https://doi.org/10.1007/s10230-007-0006-4

Knoll, P. (2016). *Induzierte seismische Ereignisse beim Anstieg des Grubenwassers in stillgelegten Bergwerken–Geomechanische Charakteristika* (Vol. 24). Leibniz Online. Retrieved from https://leibnizsozietaet.de/wp-content/uploads/2016/10/p.knoll-lo24-2016-neu-bearb.pdf

Koch, A., Jorand, R., Arnold, J., Pechnig, R., Mottaghy, D., Vogt, C., & Clauser, C. (2009). Erstellung statistisch abgesicherter thermischer und hydraulischer Gesteinseigenschaften für den flachen und tiefen Untergrund in Deutschland (Phase 2—Westliches Nordrhein-Westfalen und bayerisches Molassebecken): Schlussbericht zum BMU-Projekt FKZ 0327563.

Konietzky, H., Schütz, H., & Mittag, R. (2014). *Verbundprojekt MAGS -Konzepte zur Begrenzung der mikroseismischen Aktivität bei der energetischen Nutzung geothermaler Systeme im tiefen Untergrund.: Einzelprojekt 7: Prognose der möglichen induzierten Seismizität im Kristallin in Auswertung der flutungsbedingten Ereignisse im Bergbaurevier Aue/Schlema. Abschlußbericht des Institutes für Geotechnik über die im Projekt durchgeführten Arbeiten. Institut für Geotechnik*. TU Bergakademie Freiberg. Retrieved from https://www.mags-projekt.de/MAGS/DE/MAGS1/Einzelprojekte/EP7/EP7_node.html

Kruszewski, M., Klee, G., Niederhuber, T., & Heidbach, O. (2022). In situ stress database of the greater Ruhr region (Germany) derived from hydrofracturing tests and borehole logs. https://doi.org/10.5194/essd-2022-196

Kruszewski, M., Montegrossi, G., Backers, T., & Saenger, E. H. (2021). In situ stress state of the Ruhr Region (Germany) and its implications for permeability anisotropy. *Rock Mechanics and Rock Engineering*, *54*(12), 6649–6663. https://doi.org/10.1007/s00603-021-02636-3

Kück, J. (1988). *Hydraulic fracturing Gebirgsspannungsmessungen auf der 940 m Sohle des Ruhrkohle-Bergwerks "Haus Aden"*. [Diploma Thesis]. Ruhr-Universität Bochum.

Kunz, E. (1988). Tiefentektonik der Emscher-und Essener Hauptmulde im östlichen Ruhrgebiet: Dargestellt an der Karbonoberfläche M. 1:100 000. In *Ergänzende Beiträge zur Tiefentektonik des Ruhrkarbons:. 22 Abb., 3 Tab., 16 Taf. Geologischer Dienst Nordrhein-Westfalen—Landesbetrieb (Verlag). Tafel 1*.

Kunz, E., Wolf, R., & Wrede, V. (Eds.) (1988). *Ergänzende Beiträge zur Tiefentektonik des Ruhrkarbons: 22 Abb., 3 Tab., 16 Taf.*

Langefeld, O., & Paschedag, U. (2019). Longwall mining-development and transfer. *Mining Report Glückauf*, *155*(1), 51–72.

Lightfoot, N., & Goldbach, O. D. (1995). Controlled fault slip: Water injection: SIMRAC final project report GAP 030. *Department of Minerals and Energy*.

Liu, R., Li, B., Jiang, Y., & Huang, N. (2016). Review: Mathematical expressions for estimating equivalent permeability of rock fracture networks. *Hydrogeology Journal*, *24*(7), 1623–1649. https://doi.org/10.1007/s10040-016-1441-8

Lomax, A., Michelini, A., & Curtis, A. (2009). Earthquake location, direct, global-search methods. In R. A. Meyers (Ed.), *Encyclopedia of complexity and systems science* (pp. 1–33). Springer. https://doi.org/10.1007/978-3-642-27737-5_150-2

Lomax, A., Virieux, J., Volant, P., & Berge-Thierry, C. (2000). *Probabilistic earthquake location in 3D and layered models (advances in seismic event location)* (Vol. 18, pp. 101–134). Springer.

Loredo, C., Roqueñí, N., & Ordóñez, A. (2016). Modelling flow and heat transfer in flooded mines for geothermal energy use: A review. *International Journal of Coal Geology*, *164*, 115–122. https://doi.org/10.1016/j.coal.2016.04.013

Lu, J., Jiang, C., Jin, Z., Wang, W., Zhuang, W., & Yu, H. (2021). Three-dimensional physical model experiment of mining-induced deformation and failure characteristics of roof and floor in deep underground coal seams. *Process Safety and Environmental Protection*, *150*, 400–415. https://doi.org/10.1016/j.psep.2021.04.029

Maibaum, F. (2012). Wassertechnisches Feinkonzept zum Abschlussbetriebsplan der ZWH Ost. Report. RAG—Servicebereich Standort-und Geodienste/Markscheidewesen/Lagerstätte/Grubenwasserplanung, Herne.

McGarr, A. (1976). Seismic moments and volume changes. *Journal of Geophysical Research*, *81*(8), 1487–1494. https://doi.org/10.1029/JB081i008p01487

McGarr, A. (2014). Maximum magnitude earthquakes induced by fluid injection. *Journal of Geophysical Research: Solid Earth*, *119*(2), 1008–1019. https://doi.org/10.1002/2013JB010597

McGarr, A., Simpson, D., & Seeber, L. (2002). Case histories of induced and triggered seismicity. In *International geophysics* (Vol. 81, pp. 647–661). Academic Press. https://doi.org/10.1016/S0074-6142(02)80243-1

21699356, 2025, 9, Downloaded from https://agupubs.onlinelibrary.wiley.com/doi/10.1029/2025JB031323 by Karlsruher Institut für Technologie, Wiley Online Library on [17/09/2025]. See the Terms and Conditions (https://onlinelibrary.wiley.com/terms-and-conditions) on Wiley Online Library for rules of use; OA articles are governed by the applicable Creative Commons License

Menéndez, J., Ordóñez, A., Álvarez, R., & Loredo, J. (2019). Energy from closed mines: Underground energy storage and geothermal applications. *Renewable and Sustainable Energy Reviews*, *108*, 498–512. https://doi.org/10.1016/j.rser.2019.04.007

Meschede, M., & Warr, L. N. (2019). *The geology of Germany*. Springer International Publishing. https://doi.org/10.1007/978-3-319-76102-2

Mintrop, L. (1909a). Die Erdbebenstation der Westfälischen Berggewerkschaftskasse in Bochum, Teil 2/2. *Gluckauf*, *45*(12), 393–403.

Mintrop, L. (1909b). Die Erdbebenstation der Westfälischen Berggewerkschaftskasse in Bochum, Teil 1/2. *Gluckauf*, *45*(11), 357–366.

Mintrop, L. (1947). 100 Jahre physikalische Erdbebenforschung und Sprengseismik. *Naturwissenschaften*, *34*(10), 289–295. https://doi.org/10.1007/BF00623633

Müller, W. (1991). The stress state in the Ruhr coalfield. In *Berichte: 7. Internationaler Kongress über Felsmechanik Aachen* (pp. 1707–1711). Balkema. [16. - 20. September].

Namjesnik, D. (2021). *Origin of seismicity related to a flooded abandoned coal mining district at Gardanne, Provence, France (HAL Id:tel-03367922)*. [Doctoral Thesis]. Université de Lorraine. hal.univ-lorraine.fr. Retrieved from https://hal.univ-lorraine.fr/tel-03367922

Namjesnik, D., Kinscher, J., Contrucci, I., & Klein, E. (2022). Impact of past mining on public safety: Seismicity in area of flooded abandoned coal Gardanne mine, France. *International Journal of Coal Science & Technology*, *9*(1), 90. https://doi.org/10.1007/s40789-022-00558-1

Namjesnik, D., Kinscher, J., Gunzburger, Y., Poiata, N., Dominique, P., Bernard, P., & Contrucci, I. (2021). Automatic detection and location of microseismic events from sparse network and its application to post-mining monitoring. *Pure and Applied Geophysics*, *178*(8), 2969–2997. https://doi.org/10.1007/s00024-021-02773-4

Niederhuber, T., Kruszewski, M., Röckel, T., Rische, M., Alber, M., & Müller, B. (2023). Stress orientations from hydraulic fracturing tests in the Ruhr area in comparison to stress orientations from borehole observations and earthquake focal mechanisms. *Zeitschrift der Deutschen Gesellschaft für Geowissenschaften*, *173*(4), 625–635. https://doi.org/10.1127/zdgg/2022/0352

Niederhuber, T., Rische, M., Müller, B., Röckel, T., Allgaier, F., Fischer, K. D., et al. (2025). How can mining data be used for regional stress derivation?—Recommendations based on examples from the Ruhr Area. *Geomechanics for Energy and the Environment*, *41*, 100648. Manuscript submitted for publication. https://doi.org/10.1016/j.gete.2025.100648

Niederhuber, T., Rische, M., Röckel, T., Müller, B., & Schilling, F. (2023). *Flooding induced seismicity in the Ruhr Area—A geomechanics numerical modelling approach*. EGU23-15990. EGU General Assembly 2023 (24-28.04.2023), Vienna. https://doi.org/10.5194/egusphere-egu23-15990

Ning, S., Zhu, W., Xie, J., Song, S., Wang, X., Yu, D., et al. (2022). Influence of stress distribution in coal seams of non-uniform extremely thick key stratum and disaster-causing mechanisms. *Scientific Reports*, *12*(1), 14465. https://doi.org/10.1038/s41598-022-18641-7

Ogasawara, H., Fujimori, K., Koizumi, N., Hirano, N., Fujiwara, S., Otsuka, S., et al. (2002). Microseismicity induced by heavy rainfall around flooded vertical ore veins. In C. I. Trifu (Ed.), *Pageoph topical volumes. The mechanism of induced seismicity* (pp. 91–109). Birkhäuser. https://doi.org/10.1007/978-3-0348-8179-1_4

Park, D.-W., & Ash, N. F. (1985). Stability analysis of entries in a deep coal mine using finite element method. *Mining Science and Technology*, *3*(1), 11–20. https://doi.org/10.1016/S0167-9031(85)90066-0

Quandt, D., Rudolph, T., & Hilgers, C. (2023). Post-mining: Geomonitoring, process understanding, and utilisation of former mining areas. *Journal of Applied & Regional Geology/Zeitschrift der Deutschen Gesellschaft für Geowissenschaften (ZDGG)*, *173*(4), 507–511. https://doi.org/10.1127/zdgg/2023/0383

RAG. (2014). Konzept zur langfristigen Optimierung der Grubenwasserhaltung der RAG Aktiengesellschaft für Nordrhein-Westfalen, Herne. *RAG Aktiengesellschaft*. Retrieved from https://geodaten.rag.de/bid/tree/GenV/Grubenwasserkonzept%20NRW/Konzept_Grubenwasserhaltung.pdf

RAG. (2023). Haus Aden: Standort der Grubenwasserhaltung im Ruhrgebiet. Retrieved from https://www.rag.de/loesungen/wasserhaltung/haus-aden

RAG-BID. (2023). Ruhrkohle AG, bürger informations dienst, Grubenwasser monitoring. geodaten.rag.de. [Dataset]. Retrieved from https://geodaten.rag.de/mapapps/resources/apps/bid/index.htm

Revuzhenko, A. F. (1978). The stress-strain state of weakened rock around a working. *Soviet Mining Science*, *14*(2), 131–140. https://doi.org/10.1007/BF02499398

Rice, J. R., & Cleary, M. P. (1976). Some basic stress diffusion solutions for fluid-saturated elastic porous media with compressible constituents. *Reviews of Geophysics*, *14*(2), 227–241. https://doi.org/10.1029/RG014i002p00227

Richter, D. (1971). *Ruhrgebiet und Bergisches Land. Zwischen Wupper und Ruhr*. Gebrüder Bornträger.

Rische, M., Fischer, K. D., & Friederich, W. (2023). FloodRisk – induced seismicity by mine flooding – observation, characterisation and relation to mine water rise in the eastern Ruhr area (Germany). *Zeitschrift der Deutschen Gesellschaft für Geowissenschaften*, *173*(4), 551–564. https://doi.org/10.1127/zdgg/2023/0346

Roeloffs, E. A. (1988). Fault stability changes induced beneath a reservoir with cyclic variations in water level. *Journal of Geophysical Research*, *93*(B3), 2107–2124. https://doi.org/10.1029/JB093iB03p02107

Rothert, E., & Shapiro, S. A. (2003). Microseismic monitoring of borehole fluid injections: Data modeling and inversion for hydraulic properties of rocks. *Geophysics*, *68*(2), 685–689. https://doi.org/10.1190/1.1567239

Rudolph, T., Melchers, C., Minke, A., & Coldewey, W. G. (2010). Gas seepages in Germany: Revisited subsurface permeabilities in the German mining district. *AAPG Bulletin*, *94*(6), 847–867. https://doi.org/10.1306/10210909074

Ruhr University Bochum. (2007). *RuhrNet—Seismic network of the Ruhr-university Bochum*. Federal Institute for Geosciences and Natural Resources (BGR, Germany). Retrieved from https://www.fdsn.org/networks/detail/RN/

Schäfer, A. (2019). *Klastische sedimente* (2nd ed.). Springer. https://doi.org/10.1007/978-3-662-57889-6

Schütz, H., & Konietzky, H. (2016). Studies of flooding induced by seismicity in the Schlema-Alberoda uranium mine/Untersuchungen zur flutungsinduzierten Seismizität im Uranerzbergwerk Schlema-Alberoda. *Geomechanics and Tunnelling*, *9*(5), 508–514. https://doi.org/10.1002/geot.201600046

Senfaute, G., Chambon, C., Bigarré, P., Guise, Y., & Josien, J. P. (1997). Spatial distribution of mining tremors and the relationship to rockburst hazard. In S. Talebi (Ed.), *Seismicity associated with mines, reservoirs and fluid injections. Pageoph topical volumes*. Birkhäuser. https://doi.org/10.1007/978-3-0348-8814-1_6

Senfaute, G., Wassermann, J., & Homand, F. (2008). Induced micro-seismicity and mechanical response during the experimental flooding of an iron ore mine. In *Symposium post-mining 2008 (NC)*. ASGA. Vandoeuvre-lès-Nancy. Retrieved from https://ineris.hal.science/ineris-00973288

Shapiro, S. A., Dinske, C., Langenbruch, C., & Wenzel, F. (2010). Seismogenic index and magnitude probability of earthquakes induced during reservoir fluid stimulations. *The Leading Edge*, *29*(3), 304–309. https://doi.org/10.1190/1.3353727

Shapiro, S. A., Huenges, E., & Borm, G. (1997). Estimating the crust permeability from fluid-injection-induced seismic emission at the KTB site. *Geophysical Journal International*, *131*(2), F15–F18. https://doi.org/10.1111/j.1365-246x.1997.tb01215.x

21699356, 2025, 9, Downloaded from https://agupubs.onlinelibrary.wiley.com/doi/10.1029/2025JB031323 by Karlsruher Institut für Technologie, Wiley Online Library on [17/09/2025]. See the Terms and Conditions (https://onlinelibrary.wiley.com/terms-and-conditions) on Wiley Online Library for rules of use; OA articles are governed by the applicable Creative Commons License

Shapiro, S. A., Krüger, O. S., Dinske, C., & Langenbruch, C. (2011). Magnitudes of induced earthquakes and geometric scales of fluid-stimulated rock volumes. *Geophysics*, *76*(6), WC55–WC63. https://doi.org/10.1190/geo2010-0349.1

Shapiro, S. A., Rothert, E., Rath, V., & Rindschwentner, J. (2002). Characterization of fluid transport properties of reservoirs using induced microseismicity. *Geophysics*, *67*(1), 212–220. https://doi.org/10.1190/1.1451597

Shelly, D. R. (2024). Examining the connections between earthquake swarms, crustal fluids, and large earthquakes in the context of the 2020–2024 Noto Peninsula, Japan, earthquake sequence. *Geophysical Research Letters*, *51*(4), e2023GL107897. https://doi.org/10.1029/2023GL107897

Song, C., & Elsworth, D. (2024). Stress sensitivity of permeability in high-permeability sandstone sealed with microbially-induced calcium carbonate precipitation. *Biogeotechnics*, *2*(1), 100063. https://doi.org/10.1016/j.bgtech.2023.100063

Stech, H. J., Achatz, R., Strasser, P., Thermann, K., Caccavo, G., Gommel, U., & Kamuf, I. (2022). Construction of the new Forbach pumped storage plant. *Geomechanics and Tunnelling*, *15*(5), 469–477. https://doi.org/10.1002/geot.202200035

Suess, M. P., Drozdzewski, G. H., & Schaefer, A. (2007). Sedimentary environment dynamics and the formation of coal in the Pennsylvanian Variscan foreland in the Ruhr Basin (Germany, Western Europe). *International Journal of Coal Geology*, *69*(4), 267–287. https://doi.org/10.1016/j.coal.2006.05.003

Terzaghi, K. (1943). *Theoretical soil mechanics*. John Wiley and Sons. https://doi.org/10.1002/9780470172766

Thielemann, T. (2000). *Der Methanhaushalt über kohleführenden Sedimentbecken: das Ruhrbecken und die Niederrheinische Bucht: Das Ruhrbecken und die Niederrheinische Bucht. Methanbildung, -migration und -austausch mit der Atmosphäre (Juel-3792)*. Forschungszentrum Jülich GmbH Zentralbibliothek.

Ukelis, O., Allgaier, F., Niederhuber, T., Rettenmaier, D., & Zorn, R. (2023). Short-term soil gas measurements for fault detection—Step 1 for post-mining flooding monitoring. *Zeitschrift der Deutschen Gesellschaft für Geowissenschaften*, *173*(4), 637–651. https://doi.org/10.1127/zdgg/2022/0333

U.S. Energy Information Administration. (2023). *Annual coal report 2022*. U.S. Department of Energy. Retrieved from https://www.eia.gov/coal/annual/

Verdon, J. P., Kendall, J. M., Butcher, A., Luckett, R., & Baptie, B. J. (2017). Seismicity induced by longwall coal mining at the Thoresby Colliery, nottinghamshire, UK. *Geophysical Journal International*, *212*(2), 942–954. https://doi.org/10.1093/gji/ggx465

Voß, P. (1994). *Die Zechen in Hamm: Bildchronik der Bergwerke Heinrich Robert, Maximilian, Radbod, Sachsen* (1st ed.). Regio-Verlag Werne.

Wagner, H. (1974). Determination of the complete load-deformation characteristics of coal pillars. In *Proceedings of the 3rd international congress on rock mechanics. Symposium conducted at the meeting of Denver*.

Wagner, H. (1980). Pillar design in coal mines. *Journal of the South African Institute of Mining and Metallurgy*, *80*(1), 37–45. https://www.saimm.co.za/Journal/v080n01p037.pdf

Waldhauser, F., & Ellsworth, W. L. (2000). A double-difference earthquake location algorithm: Method and application to the Northern Hayward fault, California. *Bulletin of the Seismological Society of America*, *90*(6), 1353–1368. https://doi.org/10.1785/0120000006

Wang, H., Jiang, Y., Zhao, Y., Zhu, J., & Liu, S. (2013). Numerical investigation of the dynamic mechanical state of a coal pillar during longwall mining panel extraction. *Rock Mechanics and Rock Engineering*, *46*(5), 1211–1221. https://doi.org/10.1007/s00603-012-0337-8

Wang, S., Elsworth, D., & Liu, J. (2013). Permeability evolution during progressive deformation of intact coal and implications for instability in underground coal seams. *International Journal of Rock Mechanics and Mining Sciences*, *58*, 34–45. https://doi.org/10.1016/j.ijrmms.2012.09.005

Wang, T. A., & Dunham, E. M. (2022). Hindcasting injection-induced aseismic slip and microseismicity at the cooper basin enhanced geothermal systems project. *Scientific Reports*, *12*(1), 19481. https://doi.org/10.1038/s41598-022-23812-7

Wehling-Benatelli, S., Becker, D., Bischoff, M., Friederich, W., & Meier, T. (2013). Indications for different types of brittle failure due to active coal mining using waveform similarities of induced seismic events. *Solid Earth*, *4*(2), 405–422. https://doi.org/10.5194/se-4-405-2013

Wehling-Benatelli, S. (2010). *Clusteranalyse bergbauinduzierter Ereignisse in Hamm mit Hilfe von Wellenformähnlichkeiten - Masterthesis: Eine objektive Einteilung bergbauinduzierter seismischer Ereignisse*. [Master Thesis]. Ruhr University.

Wei, S., Avouac, J. P., Hudnut, K. W., Donnellan, A., Parker, J. W., Graves, R. W., et al. (2015). The 2012 Brawley swarm triggered by injection-induced aseismic slip. *Earth and Planetary Science Letters*, *422*, 115–125. https://doi.org/10.1016/j.epsl.2015.03.054

Wells, D. L., & Coppersmith, K. J. (1994). New empirical relationships among magnitude, rupture length, rupture width, rupture area, and surface displacement. *Bulletin of the Seismological Society of America*, *84*(4), 974–1002. https://doi.org/10.1785/BSSA0840040974

Wilson, M. P., Foulger, G. R., Gluyas, J. G., Davies, R. J., & Julian, B. R. (2017). HiQuake: The human-induced earthquake database. *Seismological Research Letters*, *88*(6), 1560–1565. https://doi.org/10.1785/0220170112

Wrede, V. (1988). Tiefentektonik der Bochumer Hauptmulde im östlichen Ruhrgebiet: Dargestellt an der Karbonoberfläche M. 1:100 000. In *Ergänzende Beiträge zur Tiefentektonik des Ruhrkarbons: 22 Abb., 3 Tab., 16 Taf. Geologischer Dienst Nordrhein-Westfalen—Landesbetrieb (Verlag). Tafel 1*.

Wynants-Morel, N., Cappa, F., De Barros, L., & Ampuero, J. P. (2020). Stress perturbation from aseismic slip drives the seismic front during fluid injection in a permeable fault. *Journal of Geophysical Research: Solid Earth*, *125*(7), e2019JB019179. https://doi.org/10.1029/2019jb019179

Yin, H., Wei, J., Lefticariu, L., Guo, J., Xie, D., Li, Z., & Zhao, P. (2016). Numerical simulation of water flow from the coal seam floor in a deep longwall mine in China. *Mine Water and the Environment*, *35*(2), 243–252. https://doi.org/10.1007/s10230-016-0385-5

Yu, Y., Chen, S.-E., Deng, K.-Z., Wang, P., & Fan, H.-D. (2018). Subsidence mechanism and stability assessment methods for partial extraction mines for sustainable development of mining cities—A review. *Sustainability*, *10*(2), 113. https://doi.org/10.3390/su10010113

Zheng, J., Zheng, L., Liu, H.-H., & Ju, Y. (2015). Relationships between permeability, porosity and effective stress for low-permeability sedimentary rock. *International Journal of Rock Mechanics and Mining Sciences*, *78*, 304–318. https://doi.org/10.1016/j.ijrmms.2015.04.025

References From the Supporting Information

DMT. (1993). Abschlussbericht Absolute Spannungsmessungen im Ruhrkarbon im Rahmen bergbaulicher Zuschnittsplanung—Gebirgsspannungen: Bericht EUR 14669 DE. Forschungsvertrag Nr. 7220-AF/129.

GD, N. R. W. (1971). *Bohrakte zur Untersuchungsbohrung Pelkum 2: Aktenzeichen: TK 4312*. Geological Survey of North Rhine-Westphalia (archive material).

Got, J.-L., Fréchet, J., & Klein, F. W. (1994). Deep fault plane geometry inferred from multiplet relative relocation beneath the south flank of Kilauea. *Journal of Geophysical Research*, *99*, 15375–15386. https://doi.org/10.1029/94JB00577

Hardebeck, J. L., & Shearer, P. M. (2002). A new method for determining first-motion focal mechanisms. *Bulletin of the Seismological Society of America*, *92*(6), 2264–2276. https://doi.org/10.1785/0120010200

21699356, 2025, 9, Downloaded from https://agupubs.onlinelibrary.wiley.com/doi/10.1029/2025JB031323 by Karlsruher Institut für Technologie, Wiley Online Library on [17/09/2025]. See the Terms and Conditions (https://onlinelibrary.wiley.com/terms-and-conditions) on Wiley Online Library for rules of use; OA articles are governed by the applicable Creative Commons License

Hardebeck, J. L., & Shearer, P. M. (2003). Using S/P amplitude ratios to constrain the focal mechanisms of small earthquakes. *Bulletin of the Seismological Society of America*, *93*(6), 2434–2444. https://doi.org/10.1785/0120020236

Hollmann, F. (2001). Methan (CH4)-Zuströmungen an der Geländeoberfläche am Beispiel des Niederrheinisch-Westfälischen Steinkohlengebietes.- Tagungsband Oberhausener Grubengas-Tage 2001, UMSICHT-Schriftenreihe Bd. (Vol. *37*, pp. 38–56).

Jaeger, J. C., Cook, N. G. W., & Zimmerman, R. W. (2007). *Fundamentals of rock mechanics* (Vol. 4). Blackwell Publ.

Jäger, B., Obermann, P., & Wilke, F. L. (1990). *Studie zur Eignung von Steinkohlenbergwerken im rechtsrheinischen Ruhrkohlenbezirk zur Untertageverbringung von Abfall-und Reststoffen: Bd. 1-4: 795 S., 55 Zeichnungen als Anlage. im Auftrag des Landesamtes für Wasser und Abfall NRW*. Düsseldorf.

Kilb, D., & Hardebeck, J. L. (2006). Fault parameter constraints using relocated earthquakes: A validation of first-motion focal-mechanism data. *Bulletin of the Seismological Society of America*, *96*(3), 1140–1158. https://doi.org/10.1785/0120040239

Michel, G. (1966). Possible origin of mineralized groundwaters in the Münster basin. *In Zeitschrift der Deutschen Geologischen Gesellschaft*, *115*(2–3), 566–571. https://doi.org/10.1127/zdgg/115/1966/566

21699356, 2025, 9, Downloaded from https://agupubs.onlinelibrary.wiley.com/doi/10.1029/2025JB031323 by Karlsruher Institut für Technologie, Wiley Online Library on [17/09/2025]. See the Terms and Conditions (https://onlinelibrary.wiley.com/terms-and-conditions) on Wiley Online Library for rules of use; OA articles are governed by the applicable Creative Commons License